PURDUE UNIVERSITY

Graduate School

This is to certify that the thesis prepared

By Cameron H.G. Wright

Entitled

"A Study of Target Enhancement Algorithms
to Counter the Hostile Nuclear Environment"

Complies with University regulations and meets the standards of the Graduate School for originality and quality

For the degree of Master of Science in Electrical Engineering

Signed by the final examining committee:

Edward J. Dulp, chair

John D. Dodenhoff

David G. Meyer

Neal C. Gallagher

Approved by the head of school or department:

May 4 1988 R.J. Schwartz

This thesis ☐ is ☒ is not to be regarded as confidential

Edward J. Dulp
Major professor

Grad. School
Form No. 9
Revised 9-85

A STUDY OF TARGET ENHANCEMENT ALGORITHMS

TO COUNTER THE HOSTILE NUCLEAR ENVIRONMENT

A Thesis

Submitted to the Faculty

of

Purdue University

by

Cameron H.G. Wright
Captain USAF

In Partial Fulfillment of the

Requirements for the Degree

of

Master of Science in Electrical Engineering

May 1988

This is dedicated to Brigadier General
Phillipe O. Bouchard, USAF (Ret) whose
guidance and advice helped me reach
this goal,

and

to Robin.

ACKNOWLEDGMENTS

I wish to thank my major professor, Edward J. Delp, whose patience, guidance, and understanding were invaluable during the preparation of this thesis. I am also indebted to Professors N. C. Gallagher, D. G. Meyer, and J. S. Sadowsky for their help as members of my Advisory Committee.

This thesis would not have been possible without the people and equipment associated with the Computer Vision and Image Processing Laboratory of the Purdue University School of Electrical Engineering. Special thanks to C. Henry Chu and Jisheng Song.

I would also like to extend my appreciation to my officemates, Bob Stevenson, Andy Laker, and Dave Beering, whose support and friendly help made my research effort much more enjoyable.

Finally, I am grateful to the U.S. Air Force Systems Command† for providing me with the opportunity to pursue this research.

---

† **Opinions, conclusions, and recommendations expressed or implied within this document are solely those of the author, and do not necessarily represent the views of the United States Air Force, the Department of Defense, or any other Government agency.**

TABLE OF CONTENTS

Page

LIST OF TABLES

LIST OF FIGURES

Figure Page

ABSTRACT

Wright, Cameron H.G. MSEE, Purdue University, May 1988. A Study of Target Enhancement Algorithms to Counter the Hostile Nuclear Environment. Major Professor: Edward J. Delp.

A necessary requirement of strategic defense is the detection of incoming nuclear warheads in an environment that may include nuclear detonations of undetected or missed target warheads. A computer model is described which simulates incoming warheads as distant endoatmospheric targets. A model of the expected electromagnetic noise present in a nuclear environment is developed using estimates of the probability distributions. Predicted atmospheric effects are also included. Various image enhancement algorithms, both linear and nonlinear, are discussed concerning their anticipated ability to suppress the noise and atmospheric effects of the nuclear environment. These algorithms are then tested, using the combined target and noise models, and evaluated in terms of the stated figures of merit.

CHAPTER 1
INTRODUCTION

1.1 THE NEED TO ENHANCE TARGET IMAGES

Digital image processing can be divided into several categories, such as image enhancement, image coding, image restoration, and image analysis. This study addresses image enhancement, which is the processing of a given digitized image to make it more suitable for a specific application.

While image enhancement has received considerable attention over the years, this study is different due to the intended application. Specifically, few researchers have set out to compare and contrast image enhancement algorithms for reducing the image degradation expected from nuclear detonations. This application is of great interest to a variety of national security organizations, particularly those concerned with strategic defense.†

A high priority for any strategic defense system is the detection of incoming nuclear warheads for targeting and interception. Such a system would most likely utilize real time digital image processing, which must be robust enough to perform well even if some warheads penetrate the defensive screen and detonate. Ignoring possible physical damage to the system, nuclear detonations present a very hostile image processing environment (Figure 1.1). This environment includes electromagnetic pulses, initial nuclear radiation (neutrons, x rays, γ rays, and debris ions), residual nuclear radiation (γ rays and β particles), thermal radiation, and the resulting atmospheric effects from the blast. Even when shielding and radiation hardened electronics are used, the nuclear environment can severely corrupt the image, inhibiting the detection of follow-on warheads. It is imperative, therefore, that some form of image enhancement be employed to counteract the degradation of the image.

---

† **To ease the dissemination and handling of this study, it was decided early on to keep it unclassified. This does not diminish the validity or utility of the information contained herein, as the data necessary to model the nuclear environment within accepted limits of uncertainty is available in the open literature.**

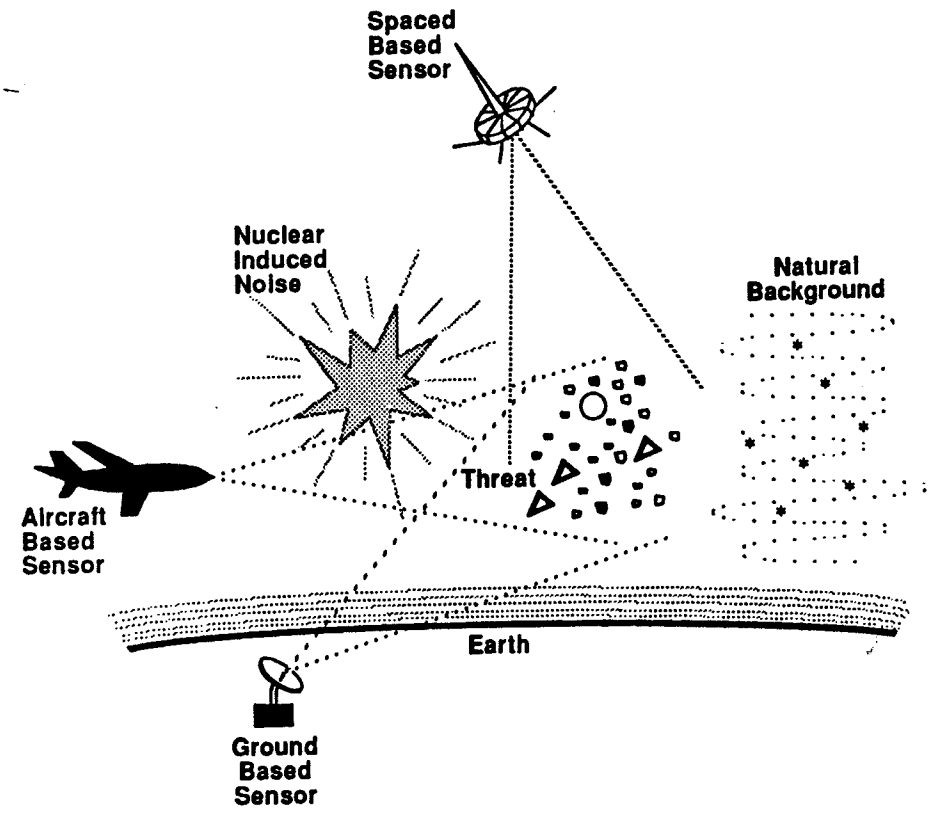

Figure 1.1 The nuclear environment.

1.2 CHOOSING APPROPRIATE ENHANCEMENT ALGORITHMS

When choosing among a variety of image enhancement algorithms, the criteria specific to the intended application must be defined. The primary criterion for this application is the ability to reduce or negate the effects of the nuclear environment. As described in Chapter 3, the two major sources of image degradation caused by nuclear detonations are impulsive noise and structured background. There are also noise sources present due to natural and man-made phenomena not related to the nuclear environment which must be considered. In the intended application, appropriate algorithms should produce minimal change in target size, shape, or position that might adversely affect the ultimate goal of the system: warhead detection and targeting. Related to this is the ability of the system to resolve multiple closely spaced objects (CSOs); thus acceptable algorithms should not blur CSOs together. Further, since any strategic defense system must operate in real time, the algorithm time and space complexity (that is, processing delay and memory

requirements) could prove to be limiting factors.

Appropriate image enhancement algorithms can be measured relative to the criteria listed above and compared for their suitability to this application. The prime focus of this study is how well the various algorithms met these criteria.

1.3 SCOPE AND ORGANIZATION OF THIS STUDY

This study compares various known image processing algorithms for their ability to enhance an image in a simulated nuclear environment. As in any study, the problem must be defined and limited in a way that makes conclusions not only useful, but also possible. In light of this, the scope of the study is outlined below.

The algorithms were selected for image enhancement only. The special requirements of other processing stages (such as detection, classification, tracking, and targeting) are not addressed. The images to be processed have no temporal information; they are assumed to be single frames from some given instant in time. Effects such as temporary sensor blinding, sensor dwell time, or apparent target movement are not modeled. While it is assumed that the sensors are of the long wavelength infrared (LWIR)† type, sensor selection is not discussed, nor is sensor location (ground, aircraft, or space based). However, the conclusions of this study are valid for a wide range of sensor types and locations. The targets are assumed to be endoatmospheric, and of uniform apparent size. A necessary assumption is that the system physically survives any initial detonation effects, such as the blast wave and thermal pulses. It is expected that the system hardware would be shielded and make maximum use of radiation hardened semiconductors; therefore, most image degradation is assumed to be a combined result of energy received by the sensor and distortions of the atmospheric medium. Some nonfatal hardware problems from radiation, such as transient bit errors, are inevitable and are modeled appropriately. Finally, it is assumed that the sources of degradation are not localized within the sensor field of view. That is, noise is not highly clustered within small areas of the image. These assumptions are justified in the following chapters.

This study is organized such that Chapters 2 and 3 focus on the target and noise models, respectively, while Chapter 4 introduces the theoretical

† ***Long wavelength infrared*** **is also called far, thermal, or emissive infrared and spans the wavelengths from 7-15 μm [56].**

aspects of the various image enhancement algorithms chosen for testing. Chapter 5 presents the results of how well the algorithms negated the effects of a simulated nuclear environment in terms of the defined figures of merit. These results are then summarized, along with the conclusions of the study, in Chapter 6.

CHAPTER 2
TARGET IMAGE CHARACTERISTICS

2.1 INTRODUCTION

Since the envisioned strategic defense system would attempt to target and intercept incoming nuclear warheads, the warheads are referred to as targets. The first phase of this study was to determine the characteristics of a target image so that it could be modeled appropriately. These characteristics are affected by target emittance properties, atmospheric transmittance, and optical limitations of the sensor front end. Since an in-depth treatment of sensor parameters is beyond the scope of this study, ideal sensors are assumed. After determining how the targets would look to a strategic defense system, digital images of simulated targets were generated as discussed below.

2.2 MODEL OF A DISTANT ENDOATMOSPHERIC TARGET

This section is largely based on previous studies by Silva [56] and Pau and El Nahas [48]. An excellent general treatment of the theory described in this section is presented in [56], with an emphasis on infrared presented in [48].

The target of interest is a ballistic reentry vehicle falling through the atmosphere. As it falls, the warhead's skin temperature rises due to friction with the increasingly dense air. The non-black body radiation, or radiant exitance, M, of the target increases according to the well known Stephan-Boltzman law, and is distributed with respect to wavelength according to its spectral radiant exitance, M_λ, curve defined by Planck's radiation law. This *thermal* radiation should not be confused with *nuclear* radiation discussed in Chapter 3. It is safe to assume that the skin temperature of the target would be somewhere between 800 K (a red-hot object) and 3000 K (a tungsten filament), which means the bulk of this radiation is in the infrared region of the electromagnetic spectrum. The background temperature of the atmosphere is around 300 K. Since M varies as the fourth power of absolute radiant temperature, the target will display a significant infrared signature against this background, distinct from other endoatmospheric objects such as aircraft.

Before the energy radiated by the hot skin of the target can reach the sensors, it is partially scattered and absorbed by the atmosphere. Atmospheric transmittance, τ, is determined by the three scattering mechanisms (Rayleigh scattering, Mie scattering, and nonselective scattering) and the molecular absorption process (primarily due to gaseous H_2O, CO_2, and O_3). These phenomena are wavelength dependent, and the spectral transmittance, τ_λ, curve is characterized by regions of high transmission (called atmospheric windows) separated by regions of low transmission. A typical τ_λ curve of the optical wavelengths is shown in Figure 2.1 for a horizontal path at sea level with a length of 1828 meters.

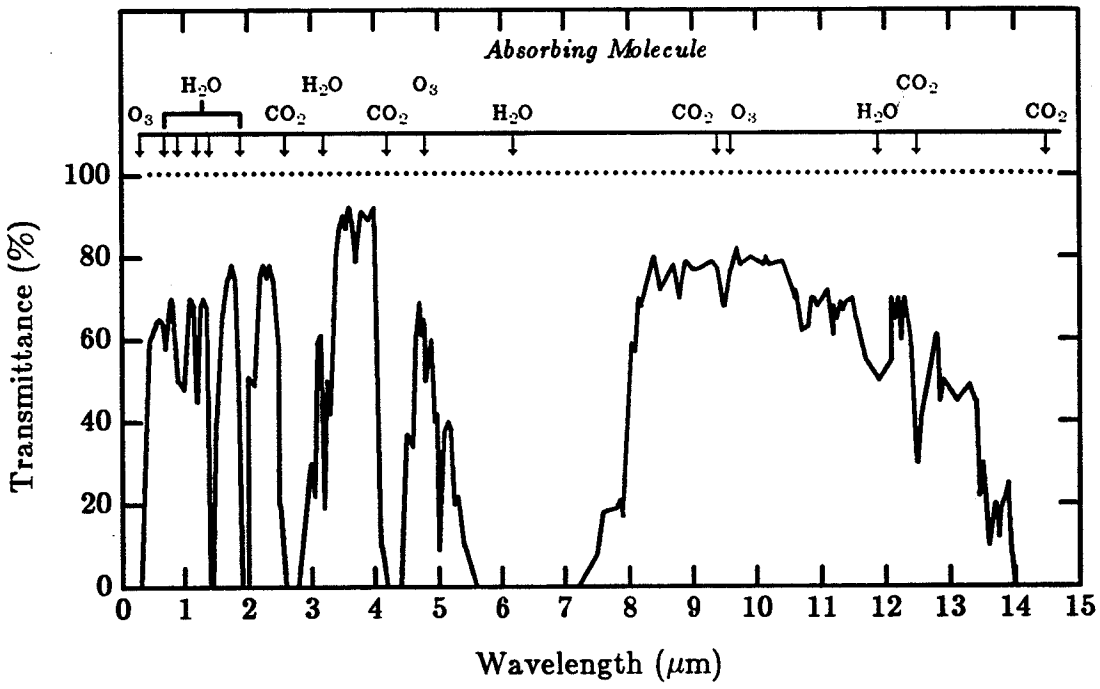

Figure 2.1 Spectral transmittance of the Earth's atmosphere for a horizontal path at sea level, length 1828 m. (adapted from [48])

As a point of reference, the human eye responds to radiation with wavelengths between 0.38 and 0.72 μm, generally referred to as the *visible* wavelengths.

While slant path and nadir path transmittance variations encountered by a strategic defense system would be somewhat different, the characteristic atmospheric windows lie in the same spectral regions. Early work in remote sensing of the optical frequencies established the boundaries of useful atmospheric windows shown in Table 2.1.

Table 2.1
Atmospheric Windows of the Optical Wavelengths
(adapted from [56])

Atmospheric Window	Spectral Region (μm)	Portion of the Electromagnetic Spectrum
1	0.3-1.3	reflective
2	1.5-1.8	reflective
3	2.0-2.6	reflective
4	3.0-3.6	†
5	4.2-5.0	†
6	7.0-15.0	emissive

† Neither reflective nor emissive radiation dominates.

These windows correspond to the peak areas of the graph in Figure 2.1. The *reflective* portion of the electromagnetic spectrum is that region in which radiation reflected off the object of interest from some external source (such as the sun) dominates; the *emissive* portion is that region in which radiation emitted by the object itself is the dominant form of radiation. Note that only window 6, in the long wavelength infrared (LWIR) region, is in the emissive portion of the spectrum. Thus window 6 is not dependent on sunlight or some other external source to sense objects. This portion of the spectrum is also unaffected by clouds, rain, and other adverse weather conditions. Since a strategic defense system must function day or night in all types of weather, and a target will emit most of its radiation in the infrared region, the most logical type of sensor to use for this purpose is the LWIR type.

Having established the properties of radiation that can be used to detect the targets, and how the atmosphere affects that radiation, the remaining factors which determine how a target should be modeled are the optical limitations of the sensor front end.

A complete description of the optical system is based on the Rayleigh-Sommerfeld propagation integral of wave optics theory, which involves the point spread function of the system [26:42-54], [48:136]. While the Rayleigh-Sommerfeld theory neglects the interactions between the electric and magnetic field vectors described by Maxwell's equations, it has been empirically shown to yield very accurate results for the type of system described here [26:32]. The target is a distant endoatmospheric object, and thus appears to the system as a partially blurred point source (sometimes referred to as an Airy disk) of LWIR. However, the blurring of the theoretical point source due to atmospheric phenomena is overwhelmed by blurring due to limitations of the optics. Thus, the point spread function of the optics determines how the point source target can be modeled.

Since it is assumed that the optics of the system will be operating far from the diffraction limits, and the incoming radiation from the target is incoherent, geometrical optics theory can be used to simplify Rayleigh-Sommerfeld predictions of optical performance. For relatively simple paraxial cases such as this, first-order approximations which ignore the effects of aberrations are commonly used for visible and near visible wavelengths. Using first-order approximations, the incoherent point spread function reduces to a first order Bessel function. But because it is very difficult to build good LWIR optics, and because the longer wavelengths result in larger blur spots for a given aberration, a more refined approach is necessary.

Third-order approximations are sufficiently exact, and predict the effects of seven types of aberration: spherical, coma, astigmatism, field curvature, distortion, axial chromatic, and off-axis chromatic. Using third-order approximations in the presence of aberrations, the incoherent point spread function becomes a very complex equation which can be solved only through numerical techniques [48:141]. This equation introduces a phase-shifting plate (the generalized pupil function) as an artifice to include aberration effects [26:121]. However, assumptions described for the sensor front end optics allow this equation to be simplified considerably. The incoherent point spread function can then be approximated by the Gaussian shaped density function [48:143]. Thus, the point source appearance of a target would become a Gaussian blur spot due to the predicted limitations of the optical system.

The ability to model a distant endoatmospheric target as a two dimensional Gaussian pulse greatly simplifies the creation of target images. Multiple target images are easily formed, and allow for more thorough testing of the image enhancement algorithms. Digital images of simulated targets were generated using bivariate Gaussian pulses as targets in a 256×256 pixel image

using 8 bit quantization. This equation has the general form of

$$f(x,y) = A\, e^{\left\{-\frac{1}{2(1-\rho^2)}\left[\frac{(x-\bar{x})^2}{\sigma_x^2} - \frac{2\rho(x-\bar{x})(y-\bar{y})}{\sigma_x\sigma_y} + \frac{(y-\bar{y})^2}{\sigma_y^2}\right]\right\}} \tag{2.1}$$

where $A = \dfrac{K}{2\pi\sigma_x\sigma_y\sqrt{1-\rho^2}}$ and K is a scaling factor.

The target pulses are scaled to have a peak value of 127 to provide sufficient dynamic range for the noise and background models added later. Using Equation (2.1), the standard deviation was set to $\sigma_x = \sigma_y = 8$ pixels and the correlation coefficient was set to $\rho = 0$, thus giving a circular appearance from the z-axis. While $\sigma_x \neq \sigma_y$ and a nonzero ρ would have yielded a more general elliptical appearance, there is little to be gained from an image enhancement point of view. The concern of this study is how well various algorithms can preserve an object of a general Gaussian shape, while reducing the effects of the nuclear environment. Elliptical targets are more general, and could be used to represent more gross aberration effects, but empirically do not provide a better measure of algorithm performance for this study. An example of a generated target image is shown in Figure 2.2. Each target image contains three targets: one relatively far from the other two for testing single target effects, and two targets close together for testing how the subsequent processing will affect the ability to resolve closely spaced objects (CSOs).

2.3 THE CLOSELY SPACED OBJECT PROBLEM

An acceptable strategic defense system must be able to distinguish between multiple targets. When several targets appear in an image, they present little problem if they are relatively distant from each other spatially. However, when this is not the case, the closely spaced targets tend to blur into each other due to the point spread function; it inhibits the ability of the system to resolve them as distinct objects. This is known as the CSO problem.

The ability to resolve two closely spaced point sources has long been used as a figure of merit for optical systems, e.g. astronomy. Several methods of quantifying this ability have been suggested in the literature; there is no general agreement about which is best for a particular application.

One measure, used in applications such as interferometers and radar systems, is the *half power point* [48]. This is the point where two pulses intersect at a distance where their respective power values (intensity values squared) are half of the peak power.

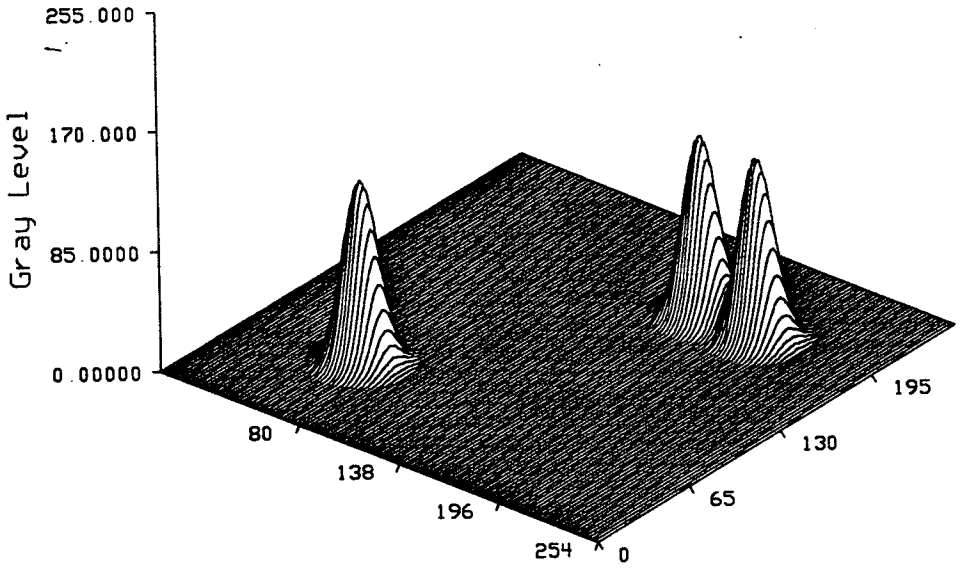

Figure 2.2 Simulated LWIR target pulses.

Another measure, used for instruments such as spectroscopes, microscopes, and telescopes, is the *Rayleigh criterion* [26]. It states that the minimum resolvable angular separation is given by

$$\theta_R = \sin^{-1}\left(\frac{1.22\lambda}{d}\right) \tag{2.2}$$

where d is the exit pupil (effective aperture) diameter, and λ is the wavelength of radiation. In the paraxial case, the approximation $\sin\theta \simeq \theta$ holds, so that Equation (2.2) becomes

$$\theta_R = 1.22\,\frac{\lambda}{d}. \tag{2.3}$$

The Rayleigh criterion is only useful for incoherent sources; a very similar measure called the *Sparrow criterion* is employed when the radiation is coherent [46]. Neither of these criteria are well suited to this study.

Another measure suggested recently [15] is the *isolation measure*, IM, which uses the concept of the *convex hull*. This is used in the processing of a binary image. An image region R is said to be *convex* if for any two points a, b of R, the straight line segment from a to b lies entirely in R. The *convex hull* of some arbitrary image region S is the smallest possible convex region that contains S, as shown in Figure 2.3.

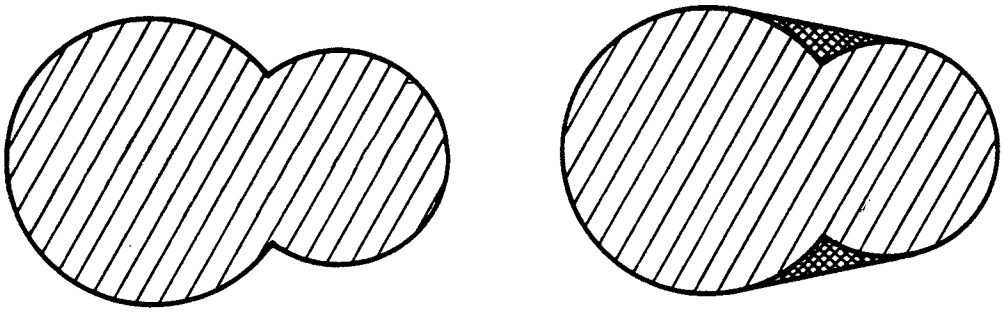

Figure 2.3 Example of a convex hull of an image region. *Left:* Original image region. *Right:* Convex hull of the image region.

An algorithm is used that computes the area of an object and the area of its convex hull, then forms the ratio

$$\text{IM} = \frac{\textit{area of the object}}{\textit{area of the convex hull}}. \tag{2.4}$$

Circular or elliptical objects such as the simulated targets of this study are convex; hence, if IM is close to one, the object is a single target. If the *IM* is much less than one, the object is most likely two or more CSOs. This measure is more sophisticated, and thereby more computationally complex, than is needed for this study.

A very simple measure exists that can be used to determine to what degree an image enhancement algorithm has blurred two CSOs together; we define this as the *CSO resolution ratio*, or CSORR. The CSORR is easily computed as

$$\text{CSORR} = \frac{\textit{minimum value between peaks}}{\textit{average of the two peak values}}. \tag{2.5}$$

In terms of the resolution threshold, if the CSORR ≤ 0.5 then the CSOs can be resolved as two targets. That is, when the peaks are twice the height (or greater) of the valley between them, they can be discerned as two distinct targets. A CSORR of 1.0 occurs when there is no valley at all (as in the case of a single target); a CSORR of 0 occurs when the valley between the peaks drops to zero (as in the case of widely separated targets). The CSORR can be measured before and after processing; ideally there should be no change. The simulated target images each contain three targets, two of which are CSOs, so that each algorithm could be evaluated on this figure of merit. Examples of cross sectional plots of target images for CSORR values of 0.25, 0.50, 0.75 and 0.90 are shown in Figures 2.4 and 2.5. The corresponding gray level images are shown in Figure 2.6.

In this chapter we have determined the predicted characteristics of an incoming warhead (the target) with regard to a strategic defense system's optics and sensor array. We then developed a realistic model that can be used to simulate an uncorrupted target image. Since the anticipated nuclear environment in which the system must operate will corrupt the target image, we investigate the sources of this corruption in the next chapter and develop appropriate models to simulate it.

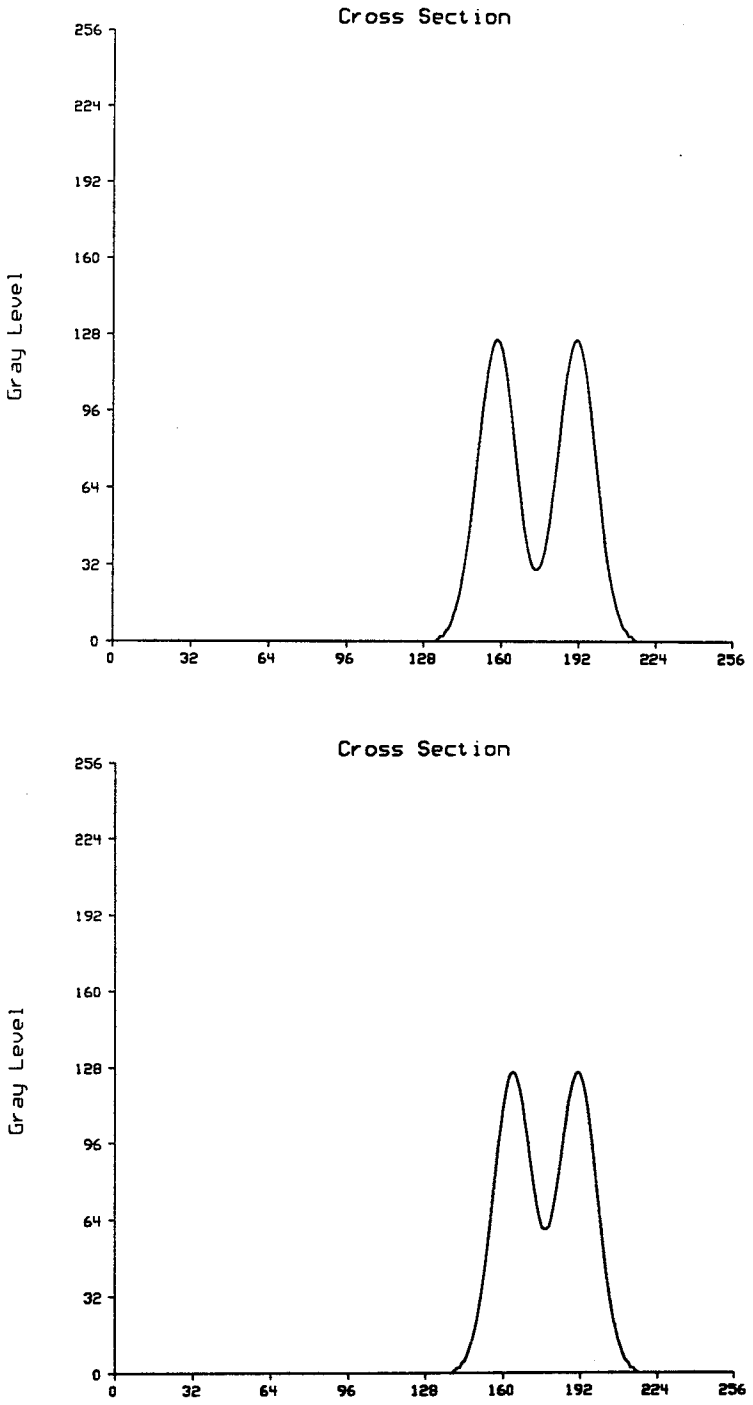

Figure 2.4 Cross sectional plot of the CSOs. *Top:* CSORR = 0.25. *Bottom:* CSORR = 0.50.

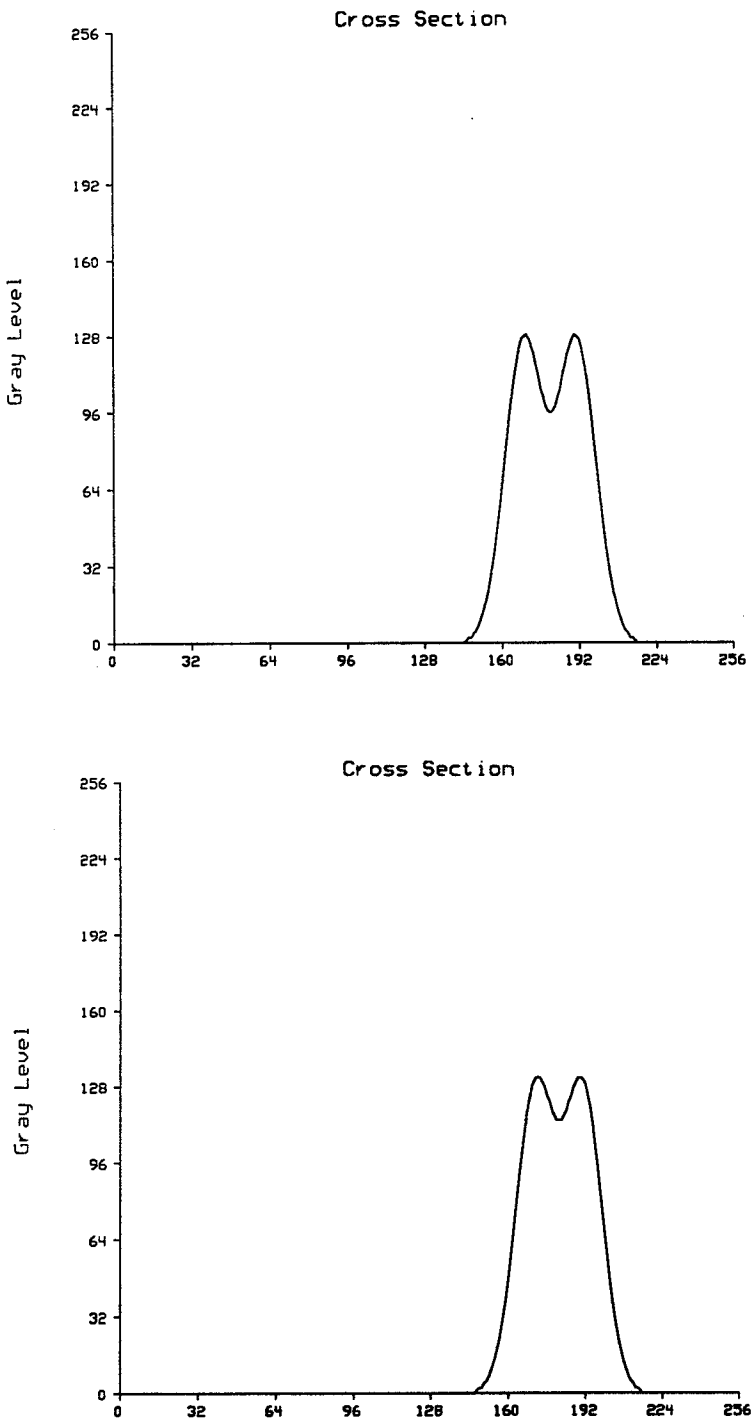

Figure 2.5 Cross sectional plot of the CSOs. *Top:* CSORR = 0.75. *Bottom:* CSORR = 0.90.

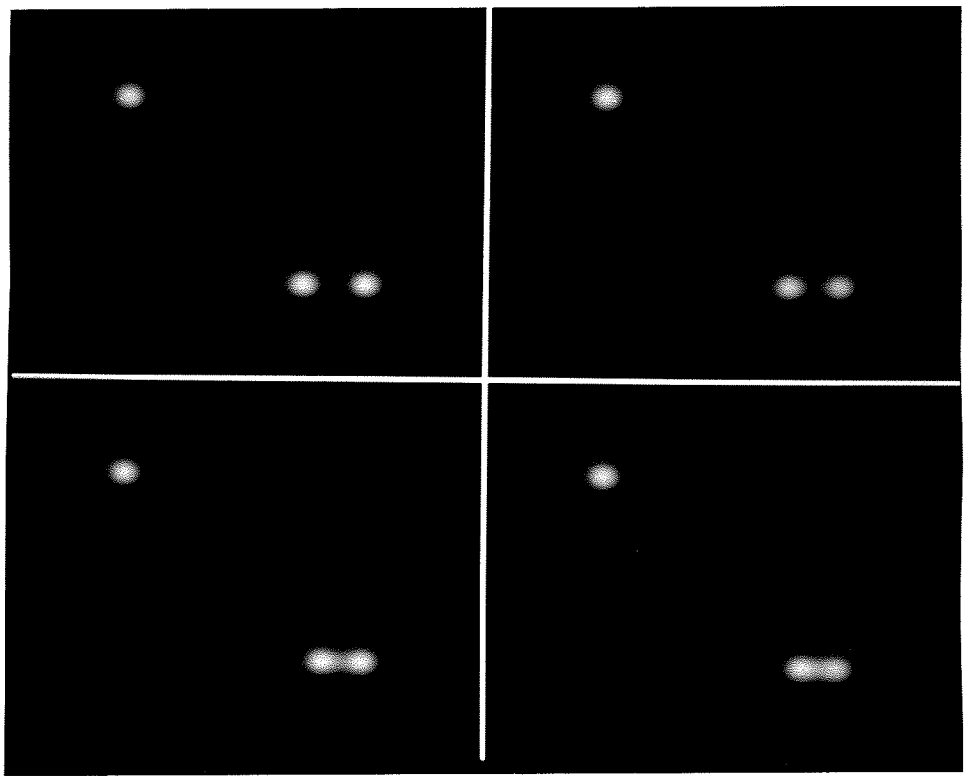

Figure 2.6 Photo of target images. CSORR equal to: **0.25** (upper left), 0.50 (upper right), 0.75 (lower left), **0.90** (lower right)

CHAPTER 3
NOISE AND BACKGROUND CHARACTERISTICS

3.1 INTRODUCTION

After defining and generating the simulated target images, the next phase of this study was to determine the characteristics of the noise and background environment. We then created a noise and background model which, when combined with the simulated target model, permitted effective testing of the various image enhancement algorithms.

Since no strategic defense system can be expected to work perfectly, some warheads may detonate before they can be intercepted and destroyed. Thus the noise and background model must take into consideration the effects of this hostile nuclear environment as well as natural sources of noise.

3.2 EFFECTS OF NUCLEAR EXPLOSIONS

This section is based mainly on information found in Glasstone and Dolan [24], one of the most complete discussions of nuclear weapons effects in the open literature.

No distinction is made here between fission and fusion weapons. The detonation effects are very similar, and modern thermonuclear devices utilize both fission and fusion mechanisms. The type of blast (e.g. exoatmospheric, high-altitude endoatmospheric, near-surface endoatmospheric, or subsurface) has the greatest effect on the phenomena associated with the detonation, but all types can contribute to the corruption of a target image.

When a nuclear explosion occurs, a complex series of events take place. A large amount of energy is liberated in a very brief period of time; the fission products, bomb casing, and other weapon parts are converted to gaseous plasma with temperatures at several tens of million degrees and accompanying pressures of millions of atmospheres in less than one microsecond. This plasma begins to emit neutrons, x rays, γ rays, and debris ions collectively termed ***initial nuclear radiation.*** For an endoatmospheric blast, the x rays are absorbed in the air immediately surrounding the detonation, and cause the formation of

a fireball, which rises like a hot air balloon at very high speed. The resulting thermal radiation has two major pulses; the first pulse peaks in the ultraviolet about one millisecond after the explosion, and the second pulse, much longer than the first, peaks in the visible and infrared after roughly half a second. The debris ions quickly interact with surrounding matter, and many of the neutrons and γ rays are absorbed by the device materials and the bomb casing. However, a considerable number of neutrons and γ rays escape the bomb debris. Some γ rays interact with the atmosphere by way of the Compton effect, producing electromagnetic pulses (EMPs) [21]. The shock wave expands quickly out from the epicenter, the radioactive cloud forms, and the fireball begins to cool. After about 1 minute, the initial nuclear radiation gives way to *residual nuclear radiation,* emitted by radioactive bomb debris and neutron-induced fallout particles. This residual nuclear radiation consists mainly of γ rays and β particles. The atmosphere is left severely ionized and contaminated with dust and debris particles, dependent upon the altitude of the blast.

For exoatmospheric blasts, no fireball is formed, and a greater percentage of the detonation energy is expended in the formation of very strong EMPs and possible ionization of the upper atmosphere. Subsurface blasts, on the other hand, produce only weak EMPs and little atmospheric ionization, but throw excessive amounts of dust and debris into the radioactive cloud.

In order to survive and perform its mission, a strategic defense system must be designed to withstand the effects of initial nuclear radiation, thermal radiation, and the shock wave [52]. The effects of the initial nuclear radiation can be subdivided into two categories: transient radiation effects on electronics (TREE) and electromagnetic pulse (EMP) [39]. Assuming no detonations occur in close proximity to the system, survivability can be reasonably assured [23],[52]. It has been shown that appropriate structural design can mitigate the effects of thermal radiation and the shock wave [24]; protective shielding can significantly reduce the EMP hazard [21],[34], and radiation hardened electronics can keep TREE to an acceptable level [39]. However, the LWIR sensors must be exposed to some degree to detect potential targets. Immediately following a blast within or near the sensor field of view, γ rays and thermal radiation will temporarily blind the sensors, but most detectors in the sensor array will quickly clear and provide image data to the system once again [15]. It is a reasonable assumption, and a necessary one for this study, that the overall system can survive the initial detonation effects with no fatal damage. As the initial effects subside, however, the system must operate effectively in an environment that includes residual nuclear radiation from one or more detonations, and any associated atmospheric effects.

3.3 IMPULSIVE NOISE

The residual nuclear radiation consists mainly of γ rays and β particles, and is generally considered to begin roughly 1 minute after detonation. The β particles are simply fast electrons emitted from radioactive nuclei isotopes; being charged, they are easily deflected and have short mean free paths. Thus, the primary cause of image corruption is due to γ rays [15]. When the γ rays (high energy photons) strike the sensor, the resulting transient ionization produces a very brief signal several orders of magnitude greater than normal for the associated image pixel, within the dynamic range limits of the sensor electronics [39]. This spike, or γ pulse, corrupts the image with *impulsive noise*. Because of its source, this noise is often referred to as γ noise.

In the hostile nuclear environment, γ noise can be a source of significant image corruption for extended periods of time. Some sensor designs, such as the impurity band conduction (IBC) shielded detector, and sampling techniques, such as spike adaptive time delay integration (SATDI), can reduce the amplitudes and event rates of γ noise, but there is no way to completely prevent it [15]. The γ noise spikes can result in both constructive and destructive interference of the target image, depending upon the associated phase relationships; this is known as *bipolar impulsive noise*.

The critical parameter that determines the level of image corruption due to γ noise is the γ radiation dose rate, commonly referred to as $\dot{\gamma}$. A mathematical model for γ noise is a random point process; in particular, γ emissions from a single source have been shown to closely approximate an inhomogeneous Poisson process in time [57] given by

$$X_t = X_0 e^{\frac{-0.693t}{\tau}}, \tag{3.1}$$

where τ is the half-life of the source isotope, X_0 is related to the quantity of the isotope, and for which

$$\dot{\gamma} = \frac{dX_t}{dt}. \tag{3.2}$$

Since the radioactive fallout results in many independent sources of γ rays, and thus many different values of τ and X_0, the dose rate $\dot{\gamma}$ cannot be accurately predicted using the derivative of Equation (3.1). Instead, a relatively accurate value of $\dot{\gamma}$ can be approximated for times ranging from about 30 minutes to

about 5,000 hours ($\simeq$ 208 days) with an empirically derived equation

$$\dot{\gamma}_t \simeq \dot{\gamma}_1 t^{-1.2} \tag{3.3}$$

where $\dot{\gamma}_t$ is the γ radiation dose rate at time t after detonation, and $\dot{\gamma}_1$ is the unit-time reference dose rate. The value of $\dot{\gamma}_1$ depends on the units in which time is expressed. For useful calculations, time is expressed in hours; thus $\dot{\gamma}_1$ would be the dose rate at 1 hour after detonation. This equation is accurate to within 25 percent for constant fallout conditions [24]. High $\dot{\gamma}$ means a high probability that a γ pulse will occur on a given pixel of a given image frame. The probability of γ contamination of a pixel is given by

$$P(\dot{\gamma}kT) = 1 - e^{-\dot{\gamma}kT} \tag{3.4}$$

where T is the sample time, k is the number of samples of the associated sensor array detectors, and $\dot{\gamma}$ is the mean dose rate over the sampling period [15]. As $\dot{\gamma}$ decreases, $P(\dot{\gamma}kT)$ also decreases. Using Equation (3.3), it can be seen that it takes 6.8 hours for the γ noise to decrease to 10 percent of the value present 1 hour after detonation, and 46.4 hours to decrease to 1 percent; $P(\dot{\gamma}kT)$ decreases even more slowly. It is assumed that during the short frame time in which a given image is formed, the decrease in $\dot{\gamma}$ suggested by Equation (3.3) is so small that $\dot{\gamma}$ can be considered to be constant [15]. Therefore, $P(\dot{\gamma}kT)$ can also be considered constant for all the pixels of a given image frame.

Whether or not a particular pixel in an image is contaminated with a γ pulse can be considered a random variable. We define the random variable $\mathbf{x}_i$ as follows: $\mathbf{x}_i = 1$ if a γ pulse has corrupted the ith pixel and $\mathbf{x}_i = 0$ otherwise. In terms of $P(\dot{\gamma}kT)$ defined above, let

$$\begin{aligned} P(\mathbf{x}_i = 1) &= P(\dot{\gamma}kT) = 1 - e^{-\dot{\gamma}kT} = p \\ P(\mathbf{x}_i = 0) &= 1 - P(\dot{\gamma}kT) = e^{-\dot{\gamma}kT} = q \end{aligned} \tag{3.5}$$

where $p = 1 - q$ and is constant for a given image. Since there are many independent sources of γ noise, the random variables $\mathbf{x}_i$ are independent. That is, the γ contamination state of a given pixel does not depend on the γ contamination state of any other pixel.

Therefore, to effectively model the corruption of a given image due to γ noise, we perform a series of N Bernoulli trials, one for each of N pixels, using the probability p, to determine which pixels contain a spike due to the γ noise. This is performed computationally by assigning the probability p, then for each pixel a pseudorandom number w is found using the C library function rand().† We first scale p such that instead of ranging from 0 to 1, the scaled value p_s ranges from 0 to $2^{31} - 1$, which is the range of w. We then compare p_s to w. Assuming equal probability of constructive or destructive interference (positive or negative spikes), and a spike amplitude so great it is hard limited by the sensor front end electronics, we set the pixel value as shown below.

$$pixel\ value = \begin{cases} no\ change & \text{if } (\mathrm{w} > p_s) \rightarrow uncorrupted \\ 255 & \text{if } (\frac{p_s}{2} \leq \mathrm{w} \leq p_s) \rightarrow positive\ spike \\ 0 & \text{if } (0 \leq \mathrm{w} < \frac{p_s}{2}) \rightarrow negative\ spike \end{cases} \tag{3.6}$$

where 255 and 0 constitute the maximum range of pixel values in the image. For convenience, we define this noise model as *type 1* impulsive noise. The value p represents the probability of pixel error, designated P_e. In Figure 3.1, the target image of Figure 2.2 has been corrupted with type 1 impulsive noise where $P_e = 0.01$. Since a large percentage of the target image has no signal, the negative spikes are difficult to discern.

The total number of spikes (positive and negative) in a given image is the random variable $\mathrm{z} = \mathrm{x}_1 + \cdots + \mathrm{x}_N$ which takes the values 0,1,...,N and $\{\mathrm{z} = k\}$ is the event k spikes out of N pixels. The random variable z is binomially distributed [47], which is defined as

$$P(\mathrm{z} = k) = \binom{N}{k} p^k q^{N-k} = \frac{N!}{k!(N-k)!}\, p^k q^{N-k}. \tag{3.7}$$

The type 1 noise model, as used in this study, actually represents two sources of image corruption. As mentioned above, it effectively models signal

† **Rand() is a multiplicative congruential pseudorandom number generator with period 2^{32} and a uniformly distributed output in the range from 0 to $2^{31} - 1$.**

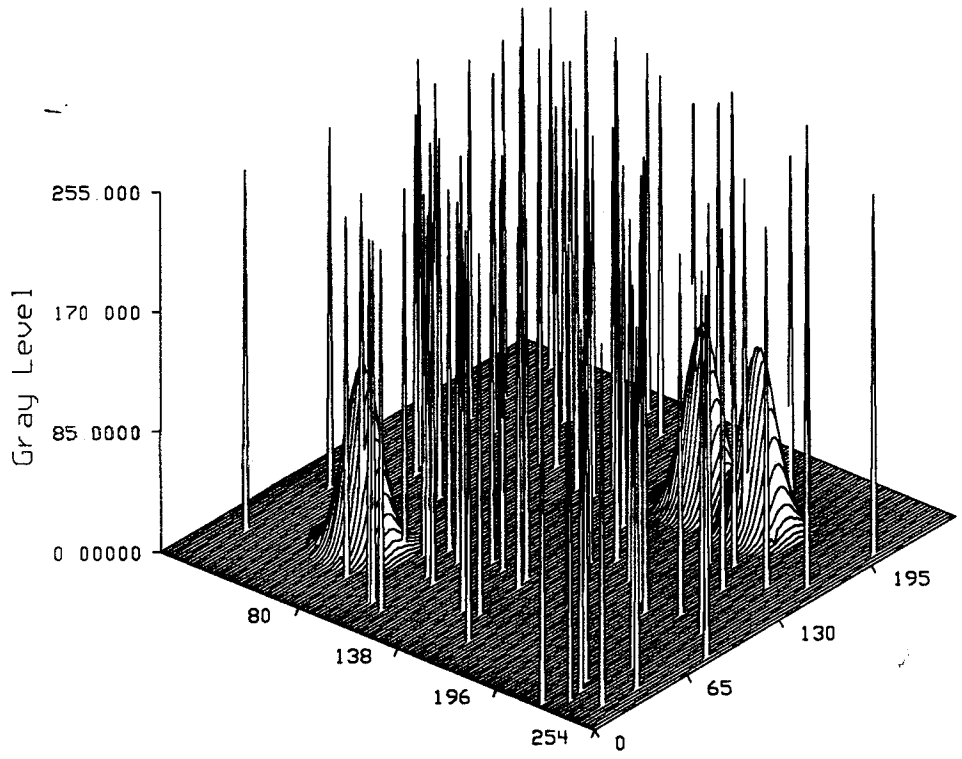

Figure 3.1 Target image corrupted with type 1 impulsive noise where $P_e = 0.01$.

spikes due to γ noise photons. It also models the result of imperfect shielding and radiation hardening of the system hardware.

No system can be made completely impervious to TREE and EMP. Proper design can significantly reduce these effects, but some hardware problems are inevitable [39]. The TREE and EMP phenomena manifest themselves most commonly in the form of latchup, upset, single-event upset (SEU), and burnout [21],[39]. Of these, latchup and SEU affect individual bits, and will be discussed later. Upset and burnout, however, generally affect an entire circuit such as a detector or its associated analog to digital (A/D) converter [39]. In terms of the front end electronics, upset and burnout would result in random pixels being set to the maximum or minimum value with equal probability [34],[39]. This is exactly the effect modeled by the type 1 impulsive noise model. While the argument for independence between pixels is not as strong in this case as it is for γ noise, any correlation between pixels would depend on factors such as exact system design and mission deployment configuration, which cannot be predicted at this time. Thus we assume for this study that

hardware effects are independent from pixel to pixel.

While the type 1 noise model reflects the majority of the γ noise corruption due to the nuclear environment, not all impulsive noise spikes will exceed the dynamic range of the front end electronics. In this case, not only will the occurrence of a spike on a pixel be random, but the amplitude and polarity of the spike will also be random. This can be effectively modeled using the concept of a *binary symmetric channel* [17],[47].

A generalized binary channel has an input $\mathbf{x}_n$ and an output $\mathbf{y}_n$ consisting of either 0 or 1. Following [47], the statistical relationship between $\mathbf{x}_n$ and $\mathbf{y}_n$ is completely specified by the input probabilities

$$P(\mathbf{x}_n = 0) = p \qquad P(\mathbf{x}_n = 1) = q \tag{3.8}$$

and the conditional probabilities

$$P(\mathbf{y}_n = j \mid \mathbf{x}_n = i) = \pi_{ij} \qquad i,j = 0,1 \tag{3.9}$$

These conditional probabilities can be put in the form of a *channel matrix* given by

$$\Pi = \begin{bmatrix} \pi_{00} & \pi_{01} \\ \pi_{10} & \pi_{11} \end{bmatrix} \tag{3.10}$$

where $\pi_{00} + \pi_{01} = 1$ and $\pi_{10} + \pi_{11} = 1$. The channel is *symmetrical* if $\pi_{10} = \pi_{01}$. The probabilities of the output states are given by

$$P(\mathbf{y}_n = 0) = \pi_{00}p + \pi_{10}q \qquad P(\mathbf{y}_n = 1) = \pi_{01}p + \pi_{11}q \tag{3.11}$$

Given the probability of error $P_e = \beta$ for a binary symmetric channel, Equation (3.10) becomes

$$\Pi = \begin{bmatrix} 1-\beta & \beta \\ \beta & 1-\beta \end{bmatrix} \tag{3.12}$$

which is represented by the diagram shown in Figure 3.2. As the diagram indicates, there is a probability β that an input bit $\mathbf{x}_n$ is corrupted such that the

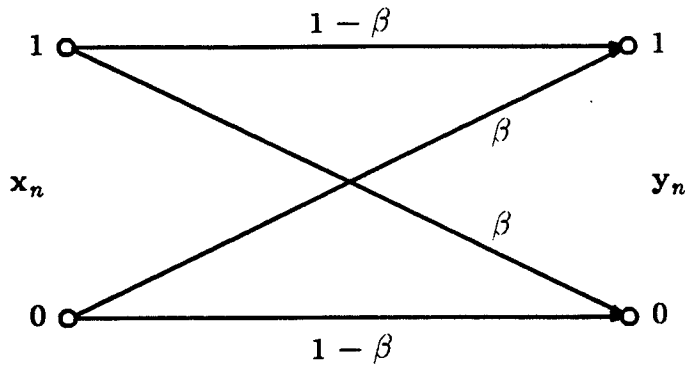

Figure 3.2 A binary symmetric channel with $P_e = \beta$.

output bit $\mathbf{y}_n$ is the complement of $\mathbf{x}_n$, and a probability $1 - \beta$ that the output will equal the input. To implement this, Bernoulli trials are performed on each *bit* of each pixel in an image. We compare β (scaled as before to β_s) to a pseudorandom number $\mathbf{w}$ and only if $\mathbf{w} \leq \beta_s$ do we complement the bit. This results in an image that is corrupted with random impulsive noise having random amplitude and polarity. We define this noise model as *type 2* impulsive noise. For an image that is formed using m bit quantization, the type 2 model will average m times as many spikes as the type 1 model, since m times as many Bernoulli trials are performed on each pixel. This must be taken into consideration when comparing P_e for type 1 and type 2 noise models. In Figure 3.3, the target image of Figure 2.2 has been corrupted with type 2 impulsive noise where $P_e = 0.001$. Since both type 1 and type 2 noise models depend upon repeated Bernoulli trials, the probability distribution of the total number of type 2 spikes $P(\mathbf{z} = k)$ is also the binomial distribution given in Equation (3.7).

Just as the type 1 noise model actually represents two sources of image corruption, γ noise and two categories of hardware problems, so does the type 2 model. It effectively simulates signal spikes due to γ noise photons that do not exceed the dynamic range of the front end electronics. But it also models TREE and EMP related hardware problems that affect individual bits (latchup and SEU). In terms of the front end electronics, latchup and SEU will most likely occur in the high density integrated circuits used for the image memory [39], and cause individual bits to be set to random states. This is exactly the effect simulated by the type 2 noise model. Since latchup and SEU generally

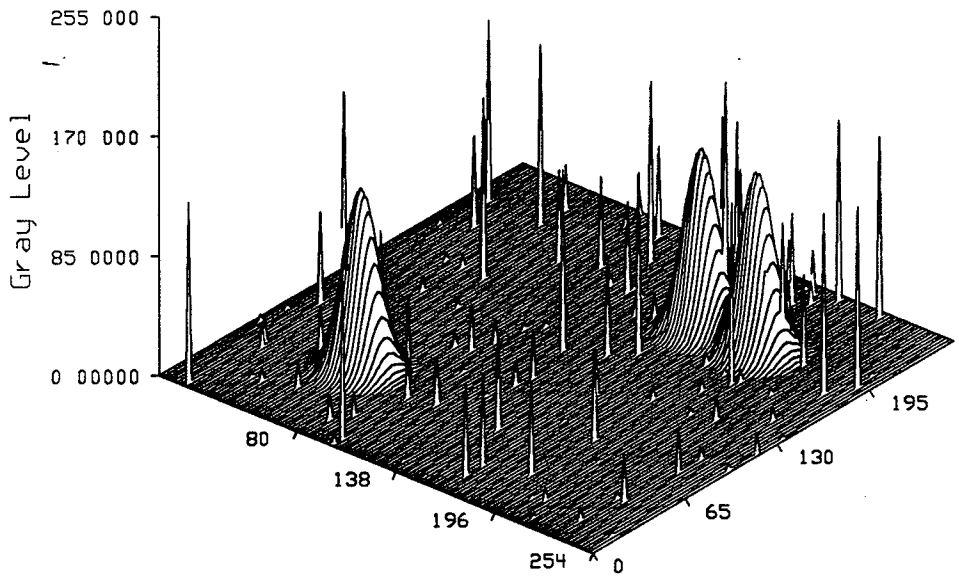

Figure 3.3 Target image corrupted with type 2 impulsive noise where $P_e = 0.001$.

corrupt a random memory cell [39], the argument for independence between bits is strong.

The combination of type 1 and type 2 noise models effectively simulates the effects of γ noise received by the sensor array, as well as anticipated nonfatal hardware problems. The nuclear environment includes another phenomenon that can severely degrade the image processing capabilities of a strategic defense system: the atmospheric effects associated with nuclear detonations. These effects can create structure in the normally uniform background.

3.4 STRUCTURED BACKGROUND

It has been suggested [15] that when multiple endoatmospheric nuclear detonations take place, the effects from the various blasts may interact to produce a spatially periodic pattern in the atmospheric transmittance. This phenomenon is known as a *structured background.* It should be emphasized that there is very little experimental data available in the open literature to base a reliable simulation; atmospheric testing of nuclear explosions was halted in 1962, and no reliable observations of multiple detonation effects have been

made. However, the effects of single endoatmospheric detonations are well documented [24], and from these we can infer a reasonable model.

The two mechanisms most likely to contribute to the formation of a structured background are atmospheric ionization and the creation of a dense aerosol from the radioactive cloud [15]. The ionization of the atmosphere results in abnormal electron densities, which effect electromagnetic propagation in two ways: it can attenuate the field strength and it can refract the wavefront [24]. The result is a decrease in the atmospheric transmittance across the entire spectrum. The radioactive cloud can also effect electromagnetic propagation. The associated dense aerosol consists of particulate matter swept into the atmosphere by the force of the blast; a near-surface detonation will yield a more dense aerosol than one at high-altitude. The sizes of the particles range from less than 0.1 μm to greater than 1.0 cm in diameter; particles in this size range have been observed to stay suspended in the atmosphere for up to 24 hours after the burst [24],[42]. These particles greatly increase the scattering of electromagnetic waves. In particular, the larger particles contribute to nonselective scattering, which attenuates electromagnetic energy independent of the wavelength [56]. Thus this mechanism also results in a decrease of the atmospheric transmittance across the entire spectrum.

These effects tend to decrease linearly over distance from the blast location [24],[42]. If only one detonation had occurred, any structuring of the background would appear in the image only as a slight linear increase, or ramping, of the background intensity in the direction away from the blast (since transmittance increases as distance from the blast increases). However, if multiple blasts had occurred, the effects could interact and create spatially periodic regions of high and low transmittance, similar to standing waves, dependent upon the relative location of the detonations to each other.† This structuring could conceivably become highly complex if many detonations occurred in close proximity. For the purposes of this study, however, the assumption is made that few blasts occurred close enough to each other to set up strong interactions and that the pattern of the structuring is sinusoidal in space. More distant blasts are assumed to add a linear ramping to the background structure. An example of this ramped sinusoidal model of a structured background using the target image of Figure 2.2 is shown in Figure 3.4. In terms of image coordinates (with units of pixels in the x and y directions, and quantizer levels in the z direction), the linear ramp has a slope of 0.4

† It is also possible that the ionization from a single blast, interacting with the Earth's magnetic field, could result in a structured background.

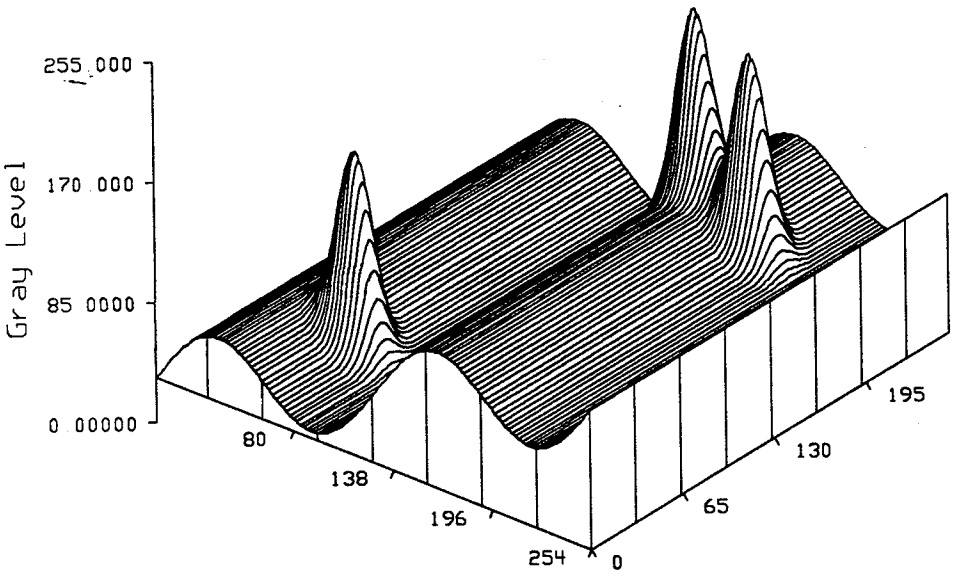

Figure 3.4 Target image with a ramped sinusoidal structured background.

levels/pixel, and the peak amplitude of the sinusoid is 32 levels, with a period of 128 pixels. Given the assumptions stated above, this is a reasonable model of the structured background that has been theorized due to interactions in a multiple detonation nuclear environment.

The three models used to simulate the image degradation due to the nuclear environment are the type 1 noise model, the type 2 noise model, and the structured background model. Even without nuclear detonations, however, noise arising from natural and man-made phenomena will be present in the images, and must be taken into consideration.

3.5 GAUSSIAN WHITE NOISE

In an environment free of nuclear detonations, there are still a large number of noise sources that can degrade images, although the intensity of this noise is much lower than the noise associated with the nuclear environment. The various types of noise arising from natural phenomena, e.g. thermal (or "Johnson"), shot, contact, and popcorn (or burst) noise, exist to some degree at all times in electronic systems [45]. The LWIR sensors may pick up some atmospheric and galactic noise in the image background [48], and the A/D converter and other digital circuitry will induce quantization noise and noise from

switching transients [17] into the image. These nonnuclear related sources of noise are generally treated as independent, random processes [11],[45]. The instantaneous value of these processes are therefore independent random variables which can only be described in terms of probability [45].

The probability density function of many of these noise sources have been defined empirically, e.g. thermal noise exhibits a Gaussian distribution [45], shot noise exhibits a Poisson distribution [47], and noise from switching transients exhibits a log-normal distribution [13]. However, we wish to define a single model to simulate the effects of all the nonnuclear related noise sources.

If we define the independent random variables associated with these noise sources as $\mathbf{x}_1, \ldots, \mathbf{x}_n$, then under conditions weak enough that we can assume they are met for this case, the *central limit theorem* [47] states that if

$$\bar{\mathbf{x}} = \frac{\mathbf{x}_1 + \cdots + \mathbf{x}_n}{\sigma\sqrt{n}} \tag{3.13}$$

then $\sigma_{\bar{x}}^2 = 1$ and we find that the probability density function of $\bar{\mathbf{x}}$, denoted by $\bar{f}(x)$ approaches as a limit for $n \longrightarrow \infty$ the relation

$$\lim_{n\to\infty} \bar{f}(x) \simeq \frac{1}{\sqrt{2\pi}}\, e^{-x^2/2} \tag{3.14}$$

This means that for large n, the sum of the independent random variables will have a Gaussian probability density function. We can make use of this result to create a model for the combined effects of all the nonnuclear related noise sources. We simulate this noise with a Gaussian distribution having a mean of 0, and further assume that the frequency distribution of the noise power is uniform. This is known as *Gaussian white noise*. This model has been proven valid empirically for a wide range of conditions [14],[45].

Computationally, we generate this using the common technique of summing 12 normalized uniformly distributed pseudorandom numbers (using the rand() function) to obtain a single Gaussian distributed random number. This technique produces a reasonable Gaussian approximation [55]. One Gaussian distributed random number is added to each pixel in the image. Figure 3.5 shows the target image of Figure 2.2 corrupted with Gaussian white noise generated as described, having a mean of 0 and a standard deviation of 32. Due to the angle of the plot, it is difficult to discern the three target pulses.

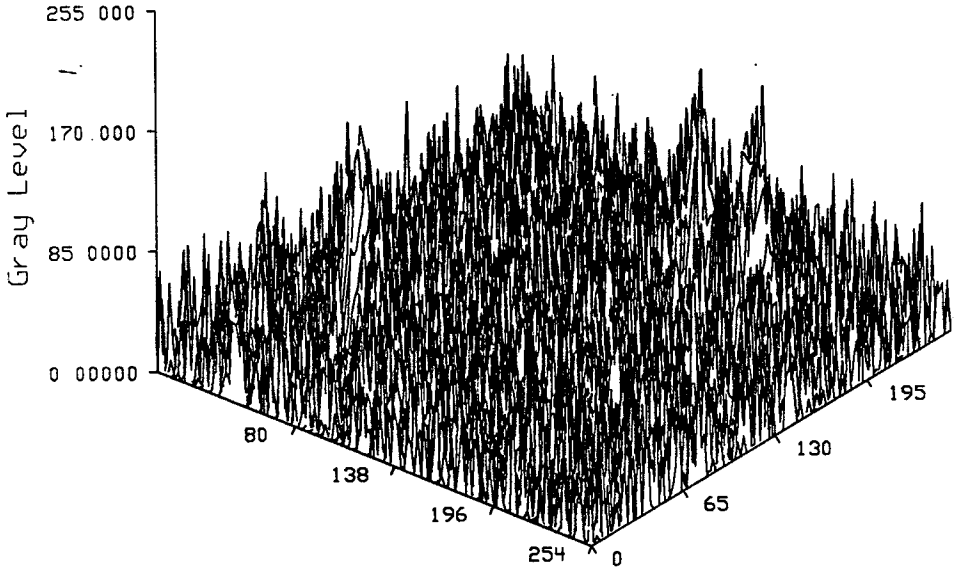

Figure 3.5 Target image corrupted with Gaussian white noise having a mean of 0 and a standard deviation of 32.

The reader may question why the random processes representing the γ noise are not included in the sum of the noise sources described above. The central limit theorem does not hold unless each summand of Equation (3.13) has a high probability of being small [8]; it also does not hold if a small number $m \ll n$ of the summand probability density functions are dominant [47]. Since the γ noise spikes are mostly very high intensity, and the associated probability density functions would dominate the sum $\bar{\mathbf{x}}$, the central limit theorem does not hold and it would be invalid to lump γ noise into all the other sources discussed above. Further, the Berry-Esseén theorem [53] asserts that the sum $\bar{\mathbf{x}}$ converges to a Gaussian probability density function at a rate $O(n^{-1/2})$; the high amplitude impulsive nature of γ noise results in a probability density function with heavy tails that exceeds the ability of $\bar{\mathbf{x}}$ to converge at that rate. Only by treating the γ noise separately, as we did using the type 1 and type 2 noise models, can we expect an accurate simulation.

Impulsive noise in an image does not lend itself easily to calculation of the signal to noise ratio (SNR); we usually specify impulsive noise in terms of the probability of error P_e. However, we can more easily define the SNR when referring to Gaussian white noise. Thus the signal to noise ratio, in dB, of a

target image corrupted with Gaussian white noise is defined as

$$\text{SNR} = 10 \log_{10} \left[\frac{(\textit{peak value of target pulse})^2}{\sigma^2} \right]. \tag{3.15}$$

The peak value of a target pulse in Figure 3.5 is $\simeq 127$ and $\sigma = 32$; thus the SNR $\simeq 12$ dB.

3.6 THE AGGREGATE NOISE MODEL

The four models defined in this chapter effectively simulate the predicted corruption of a target image in the hostile nuclear environment. The combined effects of the various sources of corruption are shown in Figure 3.6 (top), which consists of the target image of Figure 2.2 processed by the type 1 and type 2 impulsive noise models of Section 3.3, the structured background model of Section 3.4, and the Gaussian white noise model of Section 3.5. A cross sectional plot of the CSOs in the target image is shown in Figure 3.6 (bottom), and the gray level image is shown in Figure 3.7.

In this chapter, we have discussed the potential image corruption expected in the hostile nuclear environment, and have defined a set of realistic models to simulate it. In the next chapter, we discuss the theoretical aspects of the image enhancement algorithms selected for their potential to mitigate these forms of image corruption.

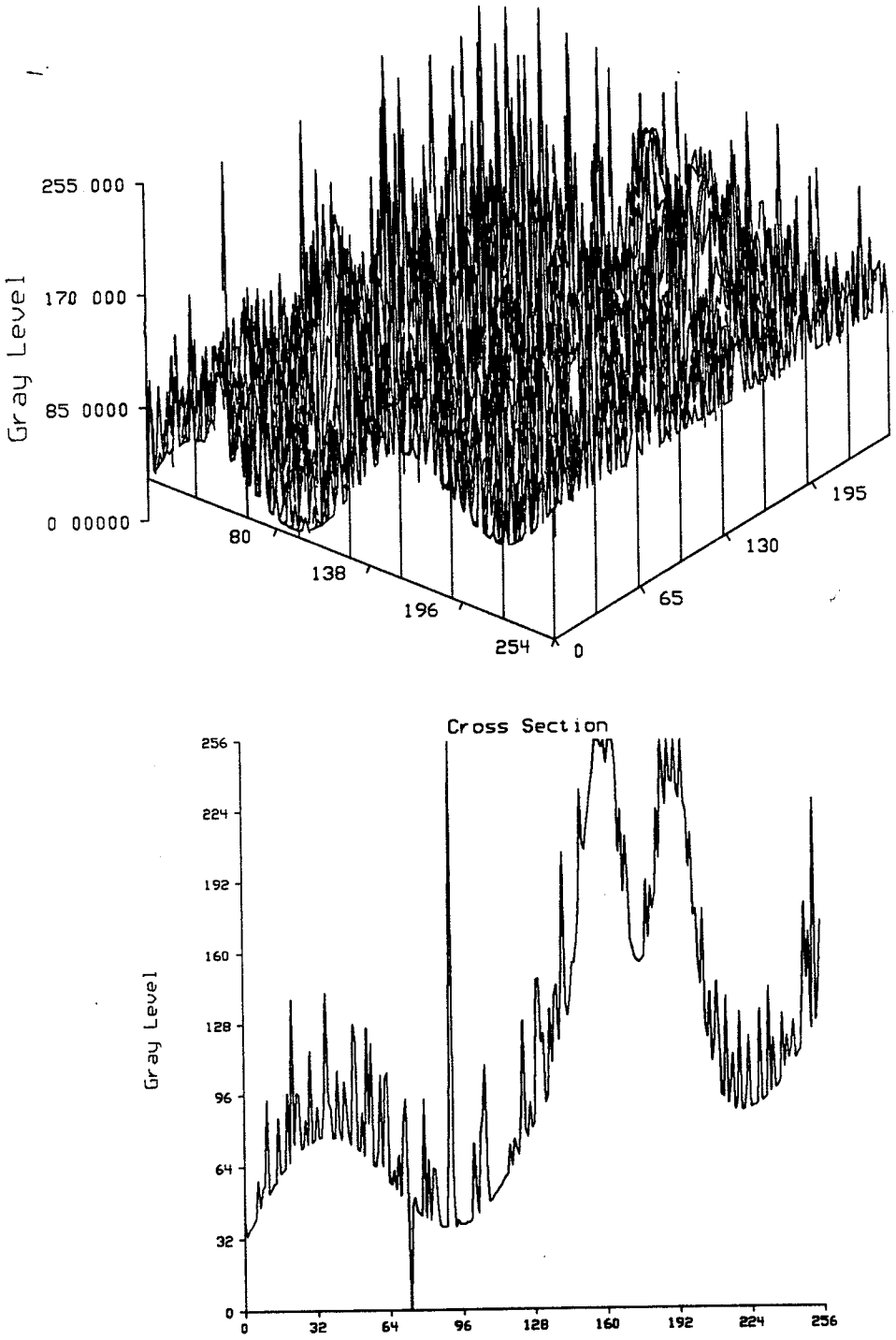

Figure 3.6 Target image corrupted by the nuclear environment. *Top:* 3-D plot. *Bottom:* Cross sectional plot of the CSOs.

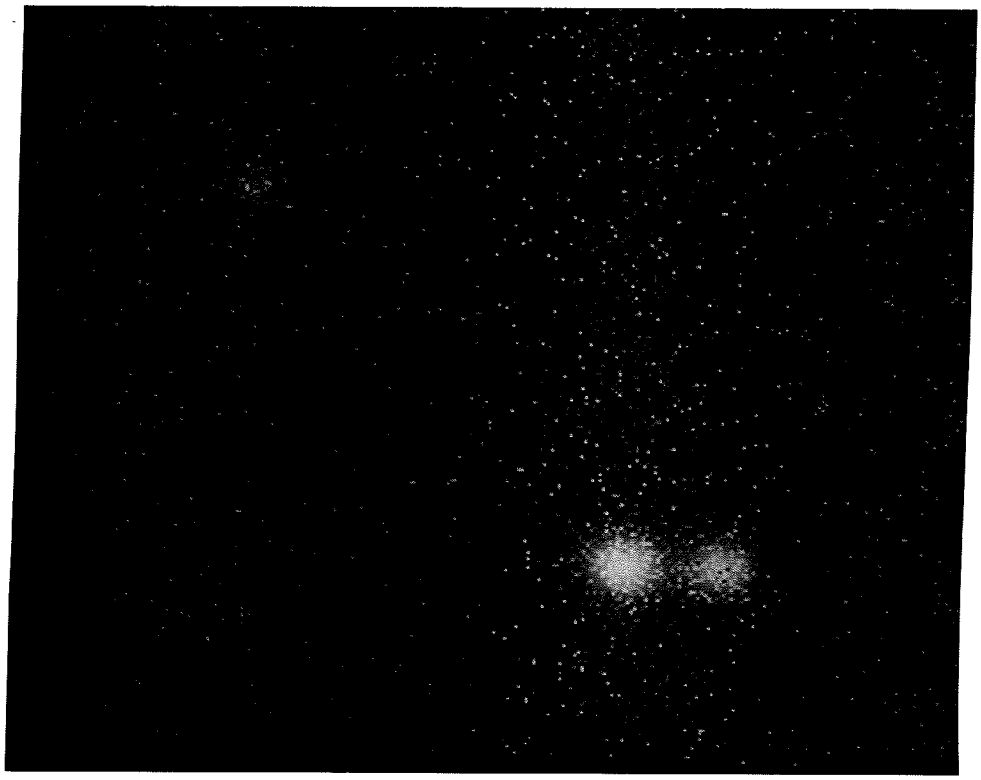

Figure 3.7 Photo of the image shown in Figure 3.6.

CHAPTER 4
IMAGE ENHANCEMENT METHODS CONSIDERED

4.1 INTRODUCTION

In the previous chapters, we have outlined the general characteristics of both the target image and the sources of image corruption that can exist in the hostile nuclear environment. We also defined realistic models we can use to simulate these phenomena. The next phase of this study was to identify candidate image enhancement algorithms.

The primary purpose of these algorithms is to remove the impulsive noise, any structured background, and the Gaussian white noise, while preserving the target pulses.† This would allow other processing stages of the strategic defense system (e.g. detection, classification, tracking, and targeting) to operate more effectively. While in some respects this can be considered a detection problem, since the algorithms must be able to detect a target pulse in order to preserve it, we consider it more of a selective filtering process.

Image enhancement approaches can be divided into two broad categories: *frequency-domain* techniques, which modify the Fourier transform of an image, and *spatial-domain* techniques, which directly manipulate the image pixel values [25]. Frequency-domain techniques present several drawbacks for this application: they are computationally intensive, the effects are global to the entire image, and they are not well suited to implementing nonlinear algorithms [44],[51]. With spatial-domain techniques, we can devise algorithms that are optimized for the pixel patterns or image areas of interest, such as the neighborhood of the target pulses [51]. Therefore, we consider only spatial-domain techniques for this study.

Spatial-domain algorithms generally operate on a limited area of adjacent pixels, known as a neighborhood or *window*, at a given time. The result of the

† Of the three, Gaussian white noise is the easiest to remove. We will therefore concentrate mainly on the more difficult problems of removing the impulsive noise and structured background.

algorithm is mapped to an output image pixel having the same coordinates as the center position of the window. The window is usually moved sequentially over the entire input image to form a complete output image. While other variations have been used, the most common window is a square window of odd size, such as 3×3, 5×5, etc.; this is the type we use for this study.† When the window is centered on a pixel near an edge of the input image, part of the window may be empty; we therefore must take this into consideration when programming the algorithm [2],[25],[51].

Spatial-domain techniques can be further divided into *linear* and *nonlinear* methods of image enhancement. Both methods were investigated for this study.

4.2 LINEAR METHODS OF IMAGE ENHANCEMENT

Historically, most image processing methods have been linear in nature [2]. Linear methods are supported by the extensive theory for linear systems (e.g. superposition), and are thus well understood and mathematically predictable.

Two common categories of linear image enhancement algorithms are those for image *sharpening* (such as the $\nabla^2 G$ filter), and those for image *smoothing* (such as the averaging filter) [51]. Sharpening techniques are used mainly to highlight the edges of objects in an image, while smoothing techniques are used primarily to reduce spurious effects such as noise [25]. Since the corrupted target image requires the removal of noise, we investigate two linear methods of smoothing the image.

4.2.1 The Gaussian Filter

A well known linear method for smoothing an image is the *Gaussian* filter, which is defined as the convolution of a Gaussian weighted window with the image [27]. This is analogous to data smoothing using Hanning or Hamming windows in signal processing to reduce side-lobe leakage problems associated with the FFT [6],[44]. The two-dimensional Gaussian window function is given [27] by

$$W(x,y) = A\ e^{-(x^2 + y^2)/2\sigma^2} \tag{4.1}$$

† The smallest window is size 1×1 where the algorithm result depends only upon the value of a single pixel; this type of algorithm is sometimes referred to as a point operation. An example of this is contrast stretching [25].

where normally $A = 1/2\pi\sigma^2$ to ensure the area under $W(x,y)$ equals one; this results in a unity gain [28]. However, convolution of two-dimensional windows over an image is a computationally intensive task.

The Gaussian shape is used in image processing because it produces acceptable smoothing while allowing relatively efficient algorithms. The smoothing of the Gaussian is considered particularly desirable by some researchers due to the Gaussian distribution's unique property of being optimally localized in both the spatial and frequency domains (that is, the best minimization of both Δx and $\Delta\omega$) [27],[38]. Efficient algorithms are possible because an n-dimensional Gaussian filter is separable into n one-dimensional filters [10]. Thus we can convolve a one-dimensional Gaussian window with each *row* of an image A to form image B, then convolve it again with each *column* of image B to form image C, which is the smoothed version of image A. This can be performed much faster than a single two-dimensional convolution. The one-dimensional Gaussian window function is given by

$$W(x) = A\ e^{-x^2/2\sigma^2} \tag{4.2}$$

where normally $A = 1/\sigma\sqrt{2\pi}$ to ensure unity gain. The convolution integral [50] for a one-dimensional continuous function $x(t)$ with the continuous window function $w(t)$ is

$$y(t) = x(t) * w(t) = \int_0^t x(u)w(t-u)\,du \tag{4.3}$$

where u is a dummy variable. The discrete case of Equation (4.3) for N data points is given [6] by

$$y_i = x_i * w_i = \sum_{k=0}^{N-1} x_k w_{i-k} \tag{4.4}$$

where k is a dummy variable. This is also the general form for a nonrecursive, or finite impulse response (FIR), digital filter [6]. Given the window shape, the Gaussian filter bears a close resemblance to a windowed FIR lowpass digital filter [28]. The reader may question why this algorithm is not performed using the FFT and multiplication in the frequency domain, a technique that has been applied in the past to image smoothing [25]. In fact, separable one-dimensional

convolution is easier and faster when using window and image sizes typical for this application [16].

The Gaussian window w_i is symmetrical, and generally much smaller in length than the image row (or column). The window size (in pixels) is determined by the standard deviation, σ, of the Gaussian; we use the smallest window size for a given σ such that the error in the coefficients is less than one percent. This results in a window approximately 7σ pixels wide in most cases. The choice of σ, and hence the window size, controls the effect the Gaussian filter has on the image.

Spatially, most pixels in an image change value gradually, except at sharp edges of objects contained in the image; noise appears as more isolated discontinuities compared to the surrounding pixel values [51]. When we convolve a number of pixels with a smooth window such as the Gaussian, abrupt variations in pixel value are reduced at the filter output. This tends to suppress the effects of noise in the output image [38]. As we increase the size of the window, an increasing number of input pixel values contribute to each output pixel value; this results in greater smoothing of the image. However, another effect of the convolution is to blur the edges of objects in the image [27]. As we increase the smoothing, we also increase the blurring. While the target pulses in this application have no sharp edges, excessive blurring of the image will tend to raise the CSORR past the threshold at which we can discern multiple targets; see Equation (2.5). This limits the window size of the Gaussian filter when used for this application, and thereby limits the amount of noise reduction we can achieve with it.

The purpose of this study is to compare image enhancement algorithms for their ability to reduce the image degradation due to nuclear detonations. Since γ noise is the dominant form of image corruption expected in the hostile nuclear environment, we are interested in how well the Gaussian filter removes impulsive spikes from an image. Unfortunately, the Gaussian filter does not perform well [28]. Being a linear operator, superposition holds, with the result that all input pixel values contribute (in proportion to the associated window coefficients) to the filter output even if one or more of the pixel values deviate greatly from the surrounding pixels. Thus a large spike, known as a *statistical outlier*, will tend to significantly affect the output value of the filter, yielding poor suppression of the spike. Additionally, there is no known method by which a Gaussian filter can selectively remove a structured background from an image [15].

While the Gaussian filter has proven useful in certain applications [27],[38], it does not seem well suited to our requirements. We next discuss a

much simpler and faster linear smoothing algorithm.

4.2.2 The Averaging Filter

The *averaging* filter (also known as the mean filter) is one of the most straightforward algorithms for image smoothing, and hence noise removal. It calculates the average (or mean) pixel value of the window, and maps that value to the appropriate pixel in the output image [25]. Given an input image with gray level pixel values $f(x,y)$, we can obtain the smoothed image $g(x,y)$ by setting the pixel values to the average value of the window region S. If we assume the window contains N pixels, and the center position of this window is at location (a,b), then the average pixel value of the window region S is found to be

$$g(a,b) = \frac{1}{N} \sum_{(x,y) \in S} f(x,y) \tag{4.5}$$

where $g(a,b)$ is mapped to the output image. This is performed for every pixel in the image $f(x,y)$.

Using the average value of the window tends to reduce spurious pixel values, and thus suppress the effects of noise [51]. The averaging operation will also tend to blur sharp edges of objects in the image in a manner comparable to the Gaussian filter. The degree to which the averaging filter smooths an image, and consequently blurs edges, is directly related to the window size chosen for the filter. A large window, by averaging over a larger number of pixels, will produce greater smoothing (and greater blurring) than a smaller window. Unfortunately, the linear operation of the averaging filter causes it to be sensitive to a single aberrant data point, much like the Gaussian filter, and similarly limits its usefulness in the presence of impulsive noise [2]. Further, the averaging filter is also unable to selectively remove a structured background from an image.

The Gaussian filter and the averaging filter are representative of linear image smoothing techniques. We noted that they share certain characteristics which may not be suitable for our intended application. In an attempt to overcome some of these limitations of the linear approach, we now investigate nonlinear methods of image smoothing.

4.3 NONLINEAR METHODS OF IMAGE ENHANCEMENT

The powerful tools associated with linear systems theory, such as superposition, allow straightforward mathematical analysis of linear methods of image enhancement. While this is a highly desirable characteristic, noise removal techniques based on linear methods (e.g. image smoothing) do not seem well suited to reducing the effects of the hostile nuclear environment. The blurring they produce adversely affects the CSORR; they perform poorly in the presence of impulsive noise; and they are unable to remove a structured background from the target image. By necessity, we depart from the mathematical elegance of linear systems theory, and examine more powerful, albeit more difficult to analyze, filtering techniques [4],[5],[20],[59].

Compared to linear filters, nonlinear filters have been shown to provide superior reduction of impulsive noise without excessive image blurring [2],[51],[54]. Selective removal of a structured background has also been demonstrated using a class of nonlinear filters [12],[15],[58]. The two categories of nonlinear algorithms most frequently applied to image filtering are those using *ranked order* operations, and those that use *morphological* operations.

4.3.1 Ranked Order Filters

Ranked order filters make use of the *order statistics* of the pixel values contained in the window [2],[9],[32]. This requires the pixel values to be sorted (or ranked) according to their respective magnitudes. If the N pixel values $x_1, \cdots, x_N$ (where N in this case is odd due to the window dimensions), are arranged in ascending order, then x_N has the largest magnitude. In keeping with the mathematical literature, we denote the ith order statistic by $x_{(i)}$. Using this notation, the *maximum* is $x_{(N)}$, the *minimum* is $x_{(1)}$, and the *median* is $x_{((N+1)/2)}$.

There are many varieties of ranked order filters [19]. In order to keep the number of filter types to be compared from becoming unwieldy, we examine only the most common implementations of each major type of ranked order filter. This means we will not explicitly discuss such variations as separable [2], signal adaptive [7],[19] or recursive [2] algorithms, nor alternative window configurations [2],[3]. The interested reader is directed to [2] and [19] for an excellent background of these variations.

4.3.1.1 The Alpha-Trimmed Mean Filter

One of the major drawbacks we noted about linear filters was their inability to effectively reduce impulsive noise. Since every pixel value contained in

the window contributed in some way to the filter output, a noise spike could not be easily suppressed. Intuitively, we realize a need to eliminate the statistical outliers contained in the window, effectively compressing the variance of the pixel values.

A *trimmed mean* is found by removing (or trimming) data points with the most extreme values, both high and low, and calculating the average of the remaining points [5]. Usually, equal numbers of high and low values are trimmed; this is known as *symmetric trimming* [19]. The number of data points removed from a sample is determined by the trimming parameter α which can range from 0 to 0.5. In equation form, the α-trimmed mean of N pixel values is given [5] by

$$X_\alpha = \frac{1}{N-2\lfloor \alpha N \rfloor} \sum_{i=\lfloor \alpha N \rfloor + 1}^{N-\lfloor \alpha N \rfloor} x_{(i)} \tag{4.6}$$

where $\lfloor\ \rfloor$ is the greatest integer function, and $x_{(i)}$ is the ith order statistic previously defined. The *α-trimmed mean* filter maps X_α to the output image for every pixel in the input image.

The most common implementation of the α-trimmed mean filter [2] is designed to operate in a manner similar to the Olympic scoring method: the highest and lowest scores are removed, and the remaining scores are averaged. Thus, $x_{(1)}$ and $x_{(N)}$ are removed, and the average of the remaining $N-2$ pixel values is mapped to the output image. This is the implementation tested for this study.

The degree of filtering is directly proportional to the window size; larger windows provide greater image smoothing. Image blurring can still be a problem when using the α-trimmed mean filter since a variation of the linear average is performed, and there is no way to remove a structured background. Also, if large window sizes are used or the impulsive noise is very heavy, more statistical outliers may appear in the window than are removed by the algorithm, reducing the effectiveness of the filter. We could adjust α upward in this case so that more spikes are removed before the average is performed, but how much is enough? It is instructive at this point to examine the algorithm at the limit values for α. Note that when we set $\alpha = 0$, Equation (4.6) is equivalent to the averaging filter defined in Equation (4.5). Further, if we set $\alpha = 0.5$, Equation (4.6) will yield the median of the window pixel values (assuming a window of odd size). Hence, the α-trimmed mean filter provides a link between the linear averaging filter and the nonlinear median filter [5].

While a simple averaging filter is sufficient in many cases where the image corruption is limited mainly to additive Gaussian noise (see Section 3.5), it has been shown that when highly impulsive noise is also present the median filter performs better [32]. Since impulsive noise predominates in the hostile nuclear environment (see Section 3.3), we next examine the median filter.

4.3.1.2 The Median Filter

The properties of *median* filters have been studied extensively in recent years (e.g., [1]-[5],[9],[18]-[20],[31],[43]). They have been shown to provide robust suppression of impulsive noise, while preserving the edges of objects in the image [20]. In addition to image processing, median filters are currently used for a diverse range of applications: from laser-imaging radar, to commercial CAT scan systems found in many hospitals, to smoothing female basal temperature charts for increasing the probability of conception [2]. We focus on a square window median filter for image enhancement.

For a window containing N pixel values, where N is odd, the median filter maps the $(N+1)/2$ order statistic to the appropriate pixel of the output image [9].† That is, if the window region S is centered on position (a,b), then the output of the filter is

$$g(a,b) = \text{median}[x_1, \cdots, x_N \mid x_i \in S] = x_{((N+1)/2)} \tag{4.7}$$

where $g(a,b)$ is the output pixel value at position (a,b), and $x_{(i)}$ is the ith order statistic of S. The median filter has many interesting properties. We briefly mention some of them here; the interested reader is directed to [1],[2], and [20] for a more complete treatment.

For odd size windows, the output of the filter is always one of the input pixel values, so that the output remains properly quantized (that is, the median filter commutes with monotonic operations) [2]. In contrast, filters that incorporate an averaging operation frequently produce output values that must be rounded or truncated in order to be requantized. Another property of the median filter is that it produces *root* images (images invariant to further median filtering) in a finite number of passes [20]. The statistical properties of

† To remain consistent with the mathematical notation for order statistics, we depart from the usual notation used in the literature of defining the dimensions of median filter windows as $(2N+1)\times(2N+1)$, in which case N would be the effective *filter order*.

the median filter are such that the median filter is very insensitive to the first-order probability distribution of the input; hence, the median filter performs well for any heavy-tailed distribution, even the Cauchy distribution [2].

The median filter produces greater smoothing as the window size is increased. Of particular interest is that the median filter does not tend to blur image edges to the degree we found for linear filters [51]. This means that the CSORR of the input image should not be adversely affected. In general, however, image objects smaller than half the dimensions of the window are eliminated by median filtering; too large a window could eliminate the target peaks we wish to preserve [2]. This property might be used advantageously; if we could eliminate only the target peaks, the remaining image would be an estimate of the background. By subtracting this estimate from the original image, we would remove any structured background. This method of *background normalization* sounds attractive in theory; however, the window sizes required to implement this are too large to be practical. Not only does processing time become a concern, but the large "flat" window would introduce significant distortion in the estimate of a structured background.† Thus, while the median filter can yield robust suppression of γ noise, it would provide a poor solution to the problem of background normalization.

In a severely corrupted image, we must resort to large windows for the median filter to achieve acceptable noise suppression [2]. However, the size of the window is limited by the smallest target pulses we desire to preserve. Additionally, both image distortion and the computational requirements increase with window size. We therefore examine filters using order statistics other than the median in an attempt to find a better solution for this application.

4.3.1.3 The Min/Max Filter

Generalized ranked order filters have been studied recently as possible alternatives to the widely used median filter [19],[32],[36]. In particular, filters known as min and max have received considerable attention concerning their ability to remove impulsive noise from an image [41],[51],[60]. The min filter maps the window minimum, or $x_{(1)}$, to the output image, while the max filter maps the window maximum, or $x_{(N)}$, to the output image.

---

† While we can use various shapes for the window, it is still only a two dimensional element. It contains no gray scale information, and thus has limited potential for geometric discrimination of nonbinary images.

Noise in an image consisting of all positive or all negative spikes is known as *unipolar impulsive noise*. If the noise density is such that over half the pixels contained in the filter window are spikes of one polarity, the median filter will map one of the spikes to the output. The obvious solution to this problem is to use a min filter for positive spikes, or a max filter for negative spikes [51]. Even under very noisy conditions, the spikes will be removed in the output image. Both the min and the max filter, when used alone, tend to distort the output image. Since the min operation is the gray level analog of the binary shrinking operation, it tends to shrink large high valued regions; conversely, the max operation is the gray level analog of the binary expanding operation, thus it tends to expand large high valued regions [41]. Therefore, the usual procedure is to cascade the min and the max together; this has the added benefit of removing bipolar impulsive noise from an image. The optimum order in which to perform the operations is determined by the characteristics of the input image; if the uncorrupted image consists of high valued objects on a low valued background, we first apply the min filter followed by the max filter, denoted as a min/max filter [51]. Conversely, a max/min filter would be best for the opposite type of image [51].

Due to the characteristics of the simulated target image (see Figure 2.2) we chose to test the min/max filter. Compared to the median filter, the min/max filter requires two passes rather than one. However, for equal noise removal, the min/max filter requires smaller windows (about half the x and y dimensions) than the median. Since this results in fewer pixel values to be ranked, the processing time compares favorably. While the min/max filter would outperform the median filter for removing unipolar impulsive noise, it seems to hold no significant advantage for removing bipolar impulsive noise (similar to γ noise).

In the same manner that the median filter tends to eliminate objects smaller than half the window size, the min/max filter tends to eliminate objects smaller than the window itself. This places a more restrictive limit on the largest useable window size compared to the median filter. However, we might use this property as discussed above for background normalization. While the smaller windows of the min/max filter alleviate to some degree the processing time constraint mentioned above for the median filter, the windows are still essentially "flat" image elements. The estimate of the structured background would thus be distorted in the same manner.

Ranked order filters, using two dimensional windows on what are effectively three dimensional gray scale images, tend to distort the shape of the image in proportion to the window size used. This distortion is usually not a

serious problem with the window sizes typically employed for noise removal. However, if we use the large windows required to remove target pulses in an effort to estimate the image background, the distortion becomes unacceptable. We seek a filter type that can remove noise as well as the median or min/max, yet uses three dimensional windows, allowing a better estimate of the background; then we may solve the background normalization problem. Fortunately, morphological filters possess the desired characteristics.

4.3.2 Morphological Filters

Morphological filters are based upon the principles of *mathematical morphology*, which permits the "quantitative description of geometric structures" [54]. These principles evolved from the combined disciplines of integral geometry and geometric probability [54], and provide an image processing approach which is based on shape [29]. Although the theory for morphological filters evolved separately, it has been shown that they can be directly related to ranked order filters [35],[36]. Traditionally, the study of ranked order filters has focused on their output statistics whereas the study of morphological filters has focused on their syntactic properties; recent research has shown that a combined approach can lead to a better understanding of both types of filters [59]. While it is beyond the scope of this text to discuss the historical background of mathematical morphology, or the detailed theoretical nature of morphological filters, the interested reader is referred to [22],[29],[35],[54], and [59] for a more complete treatment.† We first state the four principles of mathematical morphology, then examine the two basic morphological operations. We follow this with the introduction of two very useful derived operations. It is understood that many readers may be completely unfamiliar with morphological operations. For clarity, therefore, we begin with a moderately detailed discussion of morphology as applied to simple two dimensional binary images, then generalize in a more concise fashion to three dimensional gray scale images. We then proceed to examine how morphological filters can reduce the image corruption due to the hostile nuclear environment. To aid in the following discussion, some preliminary definitions are in order.

The notation $\{z\colon P\}$ is used to describe the set of points z that satisfy the property P. The translation of set A by vector b is then given by

---

† **The reader is cautioned that, to a large degree, no standard notation has yet evolved concerning mathematical morphology. While the symbols in various sources may appear similar, inspection of the individual definitions often reveal subtle, yet important, differences.**

$$A_b = \{a+b : a \in A\} \tag{4.8}$$

We define the Minkowski set addition, $A \oplus B$, of two sets A and B to be all points c such that c is the algebraic vector sum $c = a+b$, where the vectors a and b belong to sets A and B respectively [35]. A more useful algebraic interpretation of $A \oplus B$ is based on the definition of vector translation given in Equation (4.8) above. Using this, Minkowski addition is defined as the union of all translations A_b of A as the vector b sweeps set B [35]. Thus

$$A \oplus B = \{a+b : a \in A,\ b \in B\} = \bigcup_{b \in B} A_b. \tag{4.9}$$

The complement of A is designated A^c, and is equal to all points x that are *not* members of A, given [29] by

$$A^c = \{x : x \notin A\}. \tag{4.10}$$

We then define the Minkowski set subtraction of B from A, denoted $A \ominus B$, indirectly as the dual to Minkowski set addition with respect to complementation [35]. Thus

$$A \ominus B = (A^c \oplus B)^c = \bigcap_{b \in B} A_b \tag{4.11}$$

When discussing morphological methods in binary image processing, it is common to denote an object in the image as the two dimensional closed set X, and the *structuring element* as the two dimensional compact set B [35]. The structuring element is generally a much smaller and simpler set which is designed to have some predetermined geometric shape parameter [22]. We are usually interested in how well this shape parameter "fits" the image object [54]. The complement of the image object X is X^c and represents the background of the binary image. In this discussion we assume discrete (i.e. digitized) images throughout; thus where $\mathbf{R}^n$ denotes the n dimensional Euclidean space used to describe continuous images, we use $\mathbf{Z}^n$ to denote the n dimensional discrete space to describe discrete images.

Another definition that will prove useful is that of a *symmetric set*. The symmetric set $\check{B}$ with respect to the origin is related to B by the equation

$$\check{B} = \{-b : b \in B\} = \bigcup_{b \in B} \{-b\}. \tag{4.12}$$

If $B \subseteq \mathbf{R}^2$ then $\check{B}$ can be thought of as a 180° rotation of B in the $x-y$ plane. If $B \subseteq \mathbf{R}^3$ then $\check{B}$ is more difficult to visualize; by expressing every point b of the structuring element B in spherical coordinates (ρ,θ,ϕ), then $\check{B}$ can be thought of as the negation of ρ for every point b. That is, $-b$ would be located on the opposite side of an imaginary sphere centered at the origin with a radius of ρ. Thus if b is (ρ,θ,ϕ) then $-b$ is $(-\rho,\theta,\phi)$. Note that if B is symmetric about the origin, then it follows that $\check{B} = B$. For the discrete case where $B \subseteq \mathbf{Z}^n$, the descriptions of $\check{B}$ adapt in a straightforward manner. With the above definitions in mind, we now continue the discussion of mathematical morphology.

4.3.2.1 Morphological Operations

In the theory of mathematical morphology, image objects are represented by sets and are operated on by set transformations in which the image object interacts with a structuring element [35]. For a transformation to be considered a morphological operation, it must satisfy certain basic principles.

Basic Principles

The goal of mathematical morphology is the quantitative transformation of an image object. Thus we must impose certain constraints on morphological set transformations. These constraints correspond to the four basic principles of mathematical morphology: translation invariance, compatibility with change of scale, local knowledge, and upper semi-continuity [35],[54]. For a brief explanation of these principles, we use the notation $\Psi(X)$ to represent the generalized transformation of set X.

(1) *Translation invariance.* The transformation is independent of the coordinate system and the position of the origin. Thus

$$\Psi(X_z) = [\Psi(X)]_z.$$

(2) *Compatibility with change of scale.* A transformation that is independent of image magnification satisfies

$$\Psi(\lambda X) = \lambda \Psi(X), \qquad \lambda > 0.$$

This proves too restrictive to be useful for image analysis, since many operators will depend on some scale parameter λ. The principle is satisfied, however, by defining a family of transformations Ψ_λ, given by

$$\Psi_\lambda(X) = \lambda\Psi\left(\frac{X}{\lambda}\right),$$

which is independent of image magnification. This permits the transformation to be compatible with scale changes.

(3) *Local knowledge.* For any bounded mask (i.e. a spatially limited and closed frame inside of which the image is known) M_1 within which $\Psi(X)$ is desired, there is another bounded mask M_2 in which the knowledge of X is sufficient to locally perform (i.e. within M_1) the transformation. Symbolically, this given by

$$\{\forall M_1,\ \exists M_2 \mid [\Psi(X \cap M_2)] \cap M_1 = \Psi(X) \cap M_1\}$$

and thus the transformation requires only local knowledge of X. This is necessary because we always have limited knowledge of the universe, just as a photograph yields only limited knowledge of a scene.

(4) *Upper semi-continuity.* For any sequence of images X_n, where X_K contains more detail of X than X_{K-1}, we desire $\Psi(X_n)$ to be the same for all n except for some of the fine details. To satisfy this, we stipulate that Ψ is increasing and that

$$\Psi(X) = \lim_{X_n \to X} \Psi(X_n)$$

is true, where an increasing transformation has the property

$$X_1 \subset X_2 \Rightarrow \Psi(X_1) \subset \Psi(X_2).$$

For a morphological transformation to be upper semi-continuous, the structuring elements must be compact sets. This restriction also helps to satisfy the principle of local knowledge described previously.

Every set transformation satisfying the above four principles is considered to be a morphological operation [35]. We now examine the specific set transformations used to implement morphological filters.

The two fundamental operations of mathematical morphology are known as *erosion* and *dilation*; they are related to classical Minkowski set subtraction and set addition respectively [54]. From a geometric point of view, they shrink or expand a set respectively [35].

Erosion

The first morphological operation we examine is erosion, which can be viewed geometrically as a set transformation that shrinks a set. The erosion of X by B is defined as the set Z of all points z such that the translation of B by z, B_z, is contained in the original set X [59]. This is equivalent to the Minkowski set subtraction of $\check{B}$ from X [22],[35]. Thus erosion can be shown to be

$$X \ominus \check{B} = Z = \{z: B_z \subseteq X\} = \bigcap_{b \in B} X_{-b}. \tag{4.13}$$

The rationale for using $\check{B}$ in Equation (4.13) is justified as follows. We see from Equation (4.8) that $B_z = \{b+z: b \in B\}$. It can be shown [54] that as b sweeps B, the point $b+z$ lies in X if and only if z belongs to the translation X_{-b}. Equating the definition of erosion to the Minkowski subtraction defined by Equation (4.11) leads [22] to

$$\begin{aligned} \{z: B_z \subseteq X\} &= \bigcap_{b \in B} \{z: b+z \in X\} \\ &= \bigcap_{b \in B} \{z: z \in X_{-b}\} \\ &= \bigcap_{b \in B} X_{-b} = X \ominus \check{B} \end{aligned}$$

Therefore, the erosion of X by B is equivalent to the intersection of the translations of X by the elements of $\check{B}$, which, from Equation (4.11), is equal to $X \ominus \check{B}$.

It follows from above that $X \ominus B = Z$ can be stated as $Z = \{z: \check{B}_z \subseteq X\}$. Thus the Minkowski subtraction $X \ominus B$ of Equation (4.11) is the set Z of all points z such that the translation of the symmetric set $\check{B}$ by z, $\check{B}_z$, fits completely inside (i.e. is a subset of) X, whereas the erosion $X \ominus \check{B}$ involves the *direct* fitting of B (rather than $\check{B}$) inside X [22]. Note that if B is symmetric about the origin, erosion and Minkowski subtraction are equivalent [54].

A simple example that illustrates erosion in Z^2 follows. To clarify the description, we use an arbitrary cartesian coordinate system for the discrete binary image. Given

$$X = \{(-1,0),(0,0),(1,0),(-1,-1),(0,-1),(1,-1),(-1,1),(0,1),(1,1)\}$$

and

$$B = \{(0,0),(1,1)\}, \quad \text{we find that}$$

$$Z = X \ominus \check{B} = \{(-1,0),(0,0),(-1,-1),(0,-1)\}.$$

This operation is shown in Figure 4.1, where the + represents the origin of the coordinate system.

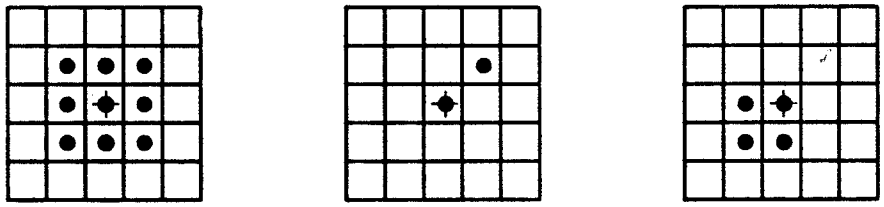

Figure 4.1 Erosion of X by B to form Z. (adapted from [35])

Computationally, there are many ways erosion can be implemented, with efficiency largely dependent on the processing hardware [29]. In one simple method, erosion is performed by sequentially moving the structuring element B over the image, which is equivalent to the translation B_z. At each location, we test for a logical AND between the elements of B_z and the image pixels that correspond to those elements. All the ANDs will be true if and only if B_z is contained entirely within some image object X, in which case the binary pixel value of 1 is mapped to the output image at the same location as the current origin of B_z. The resulting object Z in the output image is a shrunken version of X; the manner in which erosion shrinks X is dependent upon the shape of the structuring element B. Thus by designing B appropriately, we can selectively erode away certain shape features from X. Note that if B does not contain the origin, the output image may have nothing in common with the input image [29].

Erosion is similar to the familiar shrinking operation from which the min filter is derived [41]. Just as the min operation has as its dual the max operation, there exists a dual to erosion.

Dilation

We now examine dilation, the second of the two basic operations of mathematical morphology. While erosion tends to shrink a set, dilation can be thought of as a set transformation that expands a set [54]. Dilation is the dual of erosion with respect to complementation [59]. Thus

$$X \oplus \check{B} = (X^c \ominus \check{B})^c. \tag{4.14}$$

As the dual of erosion, the dilation of X by B is defined as the set Z of all points z such that the translation of B by z, B_z, intersects the original set X [35],[59]. As might be expected, this is equivalent to the Minkowski set addition X and $\check{B}$ [54]. Thus dilation can be shown to be

$$X \oplus \check{B} = Z = \{z\colon B_z \cap X \neq \varnothing\} = \bigcup_{b \in B} X_{-b}. \tag{4.15}$$

We justify the use of $\check{B}$ in Equation (4.15) as follows. From the discussion of erosion, we know that as b sweeps B, the point $b+z$ lies in X if and only if z belongs to X_{-b}; hence the point $x+z$ lies in B if and only if z belongs to B_{-x}. Equating the definition of dilation to the Minkowski addition defined by Equation (4.9) leads [22] to

$$\begin{aligned} \{z\colon B_z \cap X \neq \varnothing\} &= \{z\colon \exists x \in X \mid x \in B_z\} \\ &= \{z\colon \exists x \in X \mid x+z \in B\} \\ &= \{z\colon \exists x \in X \mid z \in B_{-x}\} \\ &= \bigcup_{x \in X} B_{-x} = \bigcup_{b \in B} X_{-b} = X \oplus \check{B} \end{aligned}$$

Therefore, the dilation of X by B is equivalent to the union of the translates of X by the elements of $\check{B}$, which, from Equation (4.9), is equal to $X \oplus \check{B}$.

It follows from above that $X \oplus B = Z$ can be stated as $Z = \{z\colon \check{B}_z \cap X \neq \varnothing\}$. Thus the Minkowski addition $X \oplus B$ of Equation (4.9) is the set Z of all points z such that the translation of the symmetric set $\check{B}$ by z,

$\check{B}_z$, partially or fully overlaps (i.e. intersects with) X, whereas the dilation $X \oplus \check{B}$ involves the *direct* fitting of B (rather than $\check{B}$) to X [22]. Note that if B is symmetric about the origin, dilation and Minkowski addition are equivalent [54].

A simple example that illustrates dilation in $\mathbf{Z}^2$ follows. As before, we use an arbitrary cartesian coordinate system for the discrete binary image. Given

$$X = \{(-1,0),(0,0),(1,0),(0,-1),(0,1)\}$$

and

$$B = \{(0,0),(0,1),(1,0)\}, \quad \text{we find that}$$

$$Z = X \oplus \check{B} = \{(-2,0),(-1,0),(0,0),(1,0),(-1,1),(0,1),(-1,-1),(0,-1),(1,-1),(0,-2)\}.$$

This operation is shown in Figure 4.2, where the + represents the origin of the coordinate system.

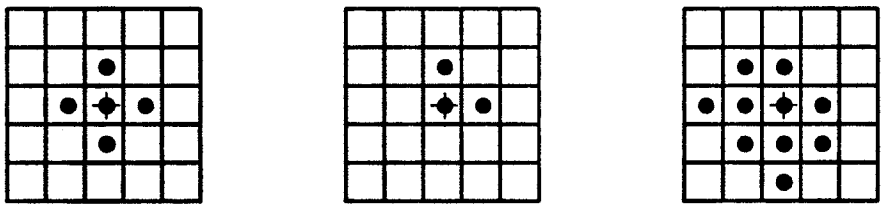

Figure 4.2 Dilation of X by B to form Z. (adapted from [35])

As was the case for erosion, there are many ways dilation can be implemented computationally, with efficiency again largely dependent on the processing hardware [29]. In one simple method, dilation is performed by sequentially moving the structuring element B over the image, which is equivalent to the translation B_z. At each location, we test for a logical OR between the elements of B_z and the image pixels that correspond to those elements. One or more ORs will be true if and only if B_z overlaps some image object X by one or more pixels, in which case the binary pixel value of 1 is mapped to the output image at the same location as the current origin of B_z. The resulting object Z in the output image is an expanded version of X; the manner in which dilation expands X is dependent upon the shape of the structuring element B. Thus by

designing B appropriately, we can selectively fill in or increase certain shape features from X. Dilation, just like erosion, may result in an output image that has nothing in common with the input image if B does not contain the origin [29].

It can be shown that erosion and dilation satisfy the four basic principles of mathematical morphology; thus they are valid morphological transformations [35],[54]. Many other theoretical properties of these transformations are presented in [22],[35] and [54]; only a few are germane to this discussion. For example, while dilation is commutative ($X \oplus \check{B} = B \oplus \check{X}$) and associative ($X \oplus (\check{B} \oplus C) = (A \oplus \check{B}) \oplus C$), erosion is not. If B contains the origin, erosion is antiextensive and dilation is extensive ($X \ominus \check{B} \subseteq X \subseteq X \oplus \check{B}$). Further, since erosion and dilation are nonlinear operators, they are in general noninvertible; this fact allows us to define another very useful pair of dual transformations derived from erosion and dilation.

Opening and Closing

If X is eroded by B, it is generally not possible to recover X completely by dilating the eroded set $X \ominus \check{B}$ by $\check{B}$. Instead, we recover a new set Z which is a somewhat simplified and less detailed version of X [35]. The exact properties of Z are dependent upon B; indeed, Z will contain only the most morphologically essential part with respect to B [54]. The transformation described is known as the *opening* of X by B, and is denoted X_B. In terms of the the basic operations of erosion and dilation, we can express opening as a derived morphological operation defined by

$$X_B = (X \ominus \check{B}) \oplus B. \tag{4.16}$$

The dual operation to opening is known as closing, denoted X^B. As expected, closing is performed by first dilating X by B, then eroding the dilated set $X \oplus \check{B}$ by $\check{B}$ [54]. We express closing as a derived morphological operation defined by

$$X^B = (X \oplus \check{B}) \ominus B. \tag{4.17}$$

The properties of opening and closing follow from the properties of erosion and dilation. We mention only those properties pertinent to this discussion; a more complete analysis is given in [22], [35] and [54]. By definition, opening and closing satisfy the four basic principles of mathematical morphology listed

above [54]. From Equation (4.14), we see that opening is the dual to closing with respect to complementation, i.e. $(X_B)^c = (X^c)^B$ and $(X^c)_B = (X^B)^c$. Thus the opening of an object in an image is the complement of closing its background. Opening is always antiextensive, while closing is always extensive; hence $X_B \subseteq X \subseteq X^B$. In contrast to erosion and dilation, both opening and closing are idempotent (stable), such that $(X_B)_B = X_B$ and $(X^B)^B = X^B$.

An example that illustrates these morphological operations is shown in Figure 4.3. The image object X is an irregular shape (a) with sharp points, narrow strips, a hole, and gaps that could be the result of noise or distortion. The structuring element B is a small disk (b) centered on the origin of an arbitrary coordinate system; thus $\check{B} = B$. Note how erosion (c) and dilation (d) respectively shrink and expand the object X. More importantly, observe how the opening (e) filters out sharp points and narrow strips, while the closing (f) fills in holes and gaps, dependent upon the relative size and shape of the structuring element.

Figure 4.3 also shows the result of following one morphological operation with another. By cascading the opening and closing (g,h), we obtain a more accurate yet smoothed estimate of the object, with both the sharp points and the small holes removed. However, note that by changing the order (g vs. h) of the cascaded operations, we obtain different results. The most accurate smoothed version of an image object would be obtained by performing both an open-close and a close-open, then averaging the results.

Up to this point, we have been discussing morphological operations with regard to binary images, which were represented as two dimensional sets. Having established the basic concepts, we can be more concise in our treatment of gray level morphology.

4.3.2.2 Gray Level Morphology

This topic has been approached from several directions in the literature: threshold decomposition [35],[59], fuzzy logic [35],[60], and the concept an umbra and surface [22],[29],[35],[54],[58] are the most common approaches. For the gray level images and gray level structuring elements we use, the umbra and surface approach seems to be the most intuitive for visualizing morphological operations in three dimensions. The theoretical analysis of gray level morphology can become quite involved. Therefore, we limit this discussion to only those general ideas necessary to understand the filter algorithm introduced in the next section. A rigorous treatment of gray level morphology would involve real analysis, topology, and set theory. Thus the reader is referred to the references cited above for greater detail than the following discussion provides.

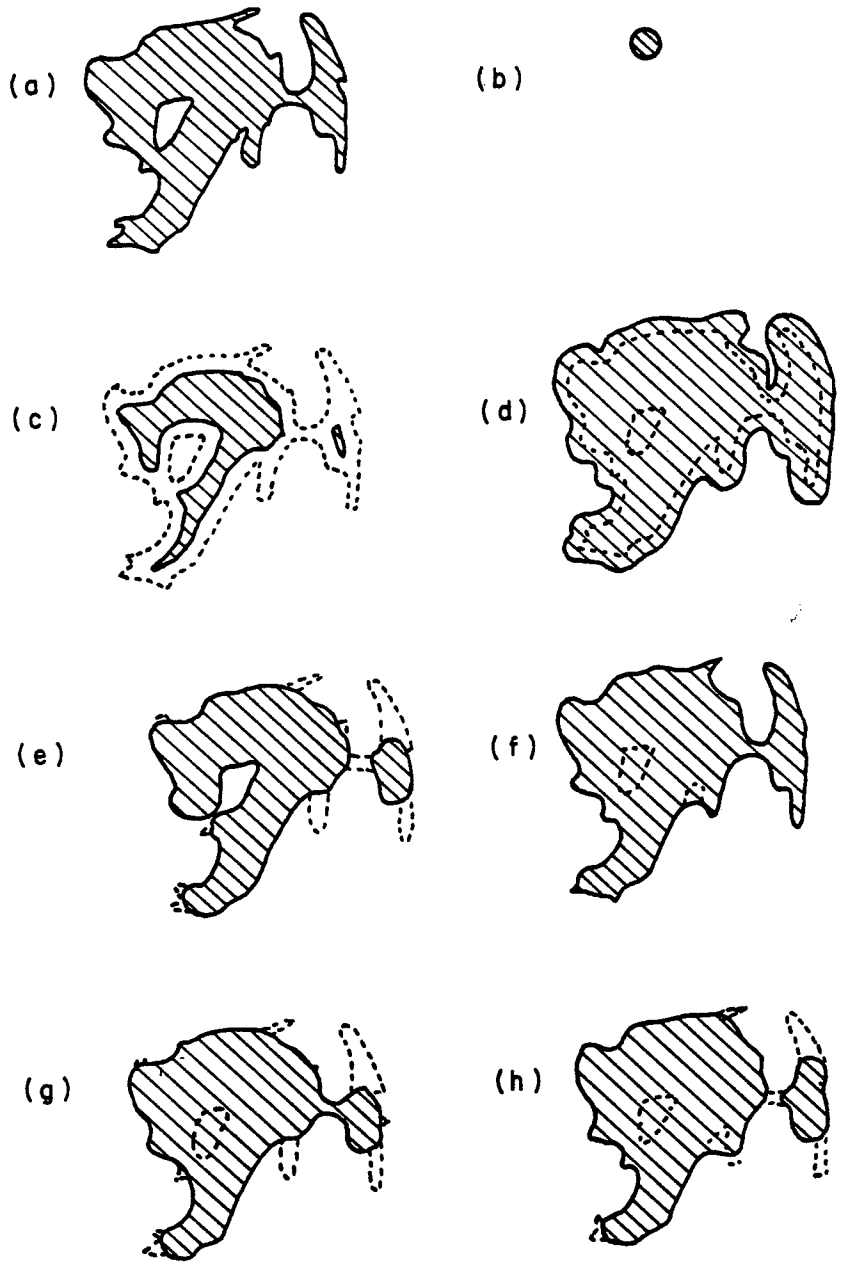

Figure 4.3 Morphological operations. (a) Image object X. (b) Structuring element B. (c) Erosion $X \ominus B$. (d) Dilation $X \oplus B$. (e) Opening X_B. (f) Closing X^B. (g) $(X^B)_B$. (h) $(X_B)^B$. (adapted from [59])

Three instances of generalized mathematical morphology are commonly used for image processing. In order of increasing complexity, they are: transformations of a set by a set (binary images and binary structuring elements), transformations of a function by a set (gray level images and "flat" binary structuring elements), and transformations of a function by a function (gray level image and gray level structuring element) [35]. We have discussed the first instance at length. Since we are most interested in the third instance for this application, we skip the second instance as a special case of the third, and proceed to discuss transformations of a function by a function.

In order to extend the morphological set transformations previously discussed to include gray level images, we must first establish some links between sets and functions. This is because mathematical morphology is defined for sets (of any dimension), whereas a gray level image is effectively a two dimensional function. That is, the image represented by $f(x,y)$ is a function defined over $(x,y) \in \mathbf{Z}^2$, such that $f(x,y)$ is the gray level (i.e. quantized intensity) of the image. Thus a graph of $f(x,y)$ versus (x,y) is three dimensional. To aid in visualization, the discrete three dimensional space of $\mathbf{Z}^3$ will be shown in the illustrations as a cross section, where the vertical axis represents the gray level and the horizontal axis represents an edge view of the $x-y$ plane. To discuss the link between sets and functions, we begin with the dual concepts of the surface of a set and the umbra of a surface [29].

A discrete three dimensional set is simply a collection of points (x,y,z) in the space of $\mathbf{Z}^3$. A solid sphere, for example, is a set of all points contained within the sphere. As with two dimensional sets, if it contains its boundary, it is closed; if it is also bounded, it is compact. Given a generalized set A, we define the *surface* of A, denoted $\mathbf{S}[A]$, to be all points (x,y,z) where z is the maximum z contained in A [22].† Thus

$$\mathbf{S}[A] = \max\{z\colon (x,y,z) \in A\}. \tag{4.18}$$

We define the *umbra* of the surface of A, denoted $\mathbf{U}[\mathbf{S}[A]]$, as the set of points (x,y,z) in $\mathbf{S}[A]$, plus all points that occupy the space below $\mathbf{S}[A]$, down to $-\infty$ [29]. Thus

† The maximum and minimum is used for discrete images in $\mathbf{Z}^n$ while the supremum (least upper bound) and infimum (greatest lower bound), respectively, is used for continuous images in $\mathbf{R}^n$.

$$\mathbf{U}[\mathbf{S}[A]] = \{(x,y,z)\colon (x,y,a) \in \mathbf{S}[A] \text{ and } z \leq a\}. \tag{4.19}$$

Note that the umbra is a three dimensional set. A generalized set A, its surface, and the umbra of its surface are shown in Figure 4.4 as a cross section.

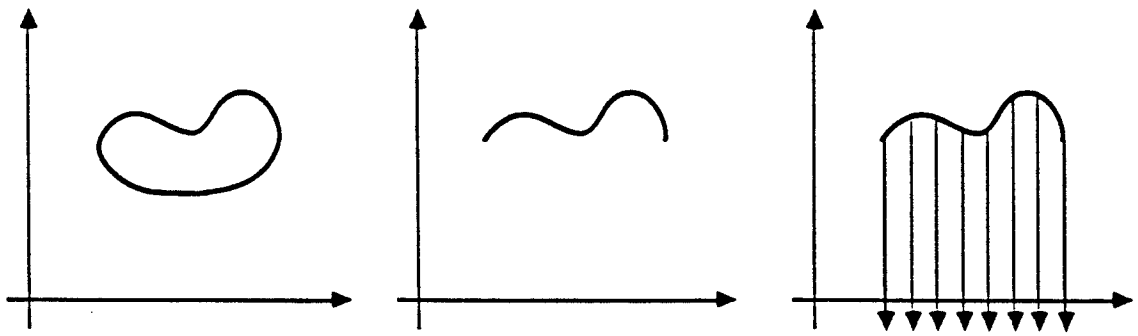

Figure 4.4 A generalized set A, its surface, and the umbra of its surface. *Left*: Set A. *Center*: $\mathbf{S}[A]$. *Right*: $\mathbf{U}[\mathbf{S}[A]]$. (adapted from [29])

Since it is understood that the umbra is defined for the surface of a set A, we usually employ the shortened notation $\mathbf{U}[A]$ for the umbra of the surface of A. If we transform a set A into its surface, and then back into a set by taking the umbra, we get a set which is unique to A but only equal to A if and only if set A was an umbra. Thus a set A is an umbra if and only if $\mathbf{U}[A] = A$ [22]. It can be shown that umbrae are idempotent, extensive, increasing, translation invariant, and compact in $\mathbf{Z}^3$ [22],[54]. Further, the morphological operations previously defined for two dimensional sets are valid for umbrae [29]. Now we relate surfaces and umbrae to two dimensional functions.

The formal definition of a function $f(x,y)$ stipulates that for a given (x,y) there is one and only one value of $f(x,y)$. While a generalized three dimensional set does not satisfy this requirement, the surface of the set does. Thus the gray level image defined by $f(x,y)$ can be represented by a surface. Indeed, the surface of a set is a function, and therefore $\mathbf{S}[f] = f$ [29]. In order to define morphological operators for gray level images, we seek transforms that will allow us to move to and from a setting in which the previously defined properties of erosion, dilation, opening, and closing are valid [22]. Since

mathematical morphology is defined for umbrae, the solution is provided by the umbra transform and the surface transform [54]. That is, we can convert two dimensional functions into three dimensional sets via the umbra transform, perform morphological operations on them, then convert them back via the surface transform [22]. This is possible because a function is uniquely represented by its umbra, and thus (if we limit the allowable sets to umbrae) the surface transform and the umbra transform are inverses of each other [22],[29],[35],[54]. For some function f, we see from above that $\mathbf{S}[\mathbf{U}[f]] = f$. Figure 4.5 illustrates this relationship in a cross sectional view.

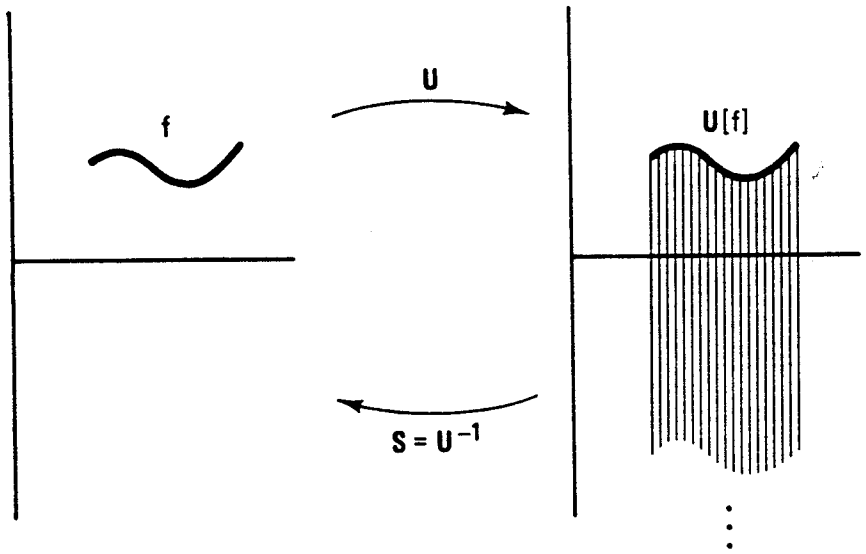

Figure 4.5 The umbra and surface inverse relationship. (adapted from [22])

We are now ready to formally state the central idea that ties functions to sets, and thus provides a homomorphism from gray level morphology to binary morphology. Given the two dimensional functions f and g, we can define Minkowski set addition and Minkowski set subtraction as

$$\mathbf{U}[f \oplus g] = \mathbf{U}[f] \oplus \mathbf{U}[g] \tag{4.20}$$

and

$$\mathbf{U}[f \ominus g] = \mathbf{U}[f] \ominus \mathbf{U}[g]. \tag{4.21}$$

These two relations are known together as the *umbra homomorphism theorem* [29]. Since umbrae are sets, the right side of Equations (4.20) and (4.21) are defined by Equations (4.9) and (4.11) respectively. From the inverse relationship of umbra and surface transforms, we see that

$$f \oplus g = \mathbf{S}[\mathbf{U}[f] \oplus \mathbf{U}[g]] = \mathbf{S}[\mathbf{U}[f] \oplus \mathbf{U}[g]] \tag{4.22}$$

and

$$f \ominus g = \mathbf{S}[\mathbf{U}[f \ominus g]] = \mathbf{S}[\mathbf{U}[f] \ominus \mathbf{U}[g]]. \tag{4.23}$$

Since the definition of a symmetric set given by Equation (4.12) is valid for a set of any dimension, we can define erosion and dilation of function f by function g in a similar manner. If f represents the gray level image, and g represents the gray level structuring element, then erosion is defined [54] as

$$f \ominus \check{g} = \mathbf{S}[\mathbf{U}[f] \ominus \check{\mathbf{U}}[g]] \tag{4.24}$$

and dilation as

$$f \oplus \check{g} = \mathbf{S}[\mathbf{U}[f] \oplus \check{\mathbf{U}}[g]]. \tag{4.25}$$

We can thus derive [54] the definition of opening as

$$f_g = (f \ominus \check{g}) \oplus g \tag{4.26}$$

and closing as

$$f^g = (f \oplus \check{g}) \ominus g. \tag{4.27}$$

Properties of the gray level morphological operations parallel the basic properties previously described for the binary case.

For computational purposes, we desire definitions of gray level mophological operators which lend themselves more easily to a digital implementation. Recall from Equations (4.13) and (4.15) that erosion and dilation, being based on Minkowski set subtraction and Minkowski set addition respectively, can be defined in terms of intersections and unions of translated sets. Observe in Figure 4.6 the effect of the union and intersection of the umbrae of f and g. Note that the surface of the union of $\mathbf{U}[f]$ and $\mathbf{U}[g]$ equals the maximum of f and g, while the surface of the intersection of $\mathbf{U}[f]$ and $\mathbf{U}[g]$ equals the minimum of f and g. This relationship allows us to define erosion and dilation in a

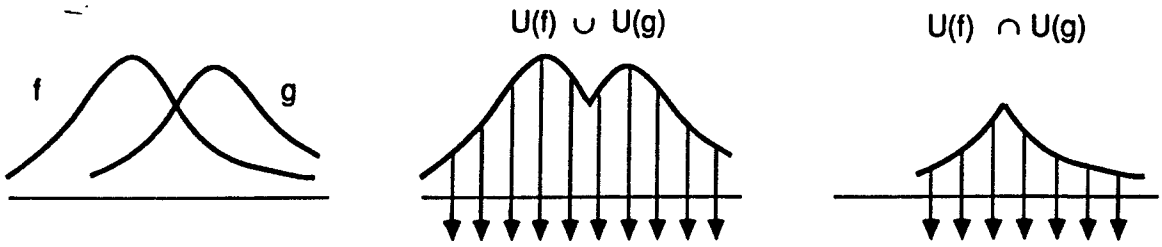

Figure 4.6 Union and intersection of umbrae. *Left*: Functions f and g. *Center*: $\mathbf{U}[f] \cup \mathbf{U}[g]$. *Right*: $\mathbf{U}[f] \cap \mathbf{U}[g]$.

straightforward algebraic form. Given $\mathbf{D}_f$ as the spatial domain in $\mathbf{Z}^2$ over which the gray level image $f(x,y)$ exists, we define [35] the erosion of f by g as

$$f \ominus \check{g} = \min_{(a,b) \in \mathbf{D}_f} \{f(a,b) - g(a-x, b-y)\} \tag{4.28}$$

and the dilation of f by g as

$$f \oplus \check{g} = \max_{(a,b) \in \mathbf{D}_f} \{f(a,b) + g(a-x, b-y)\}. \tag{4.29}$$

The opening and closing can be easily derived from this by referring to Equations (4.26) and (4.27). The opening of a gray level image can be visualized as sliding the structuring element along the surface of the image from beneath; the result is a mapping of the highest points reached by any part of the structuring element [12]. Conversely, the closing of a gray level image can be visualized as sliding a "flipped over" version of the structuring element along the surface of the image from above; the result is a mapping of the lowest points reached by any part of the structuring element [12].

To illustrate these operations, we provide some simple examples. In Figure 4.7, a cross sectional view of gray level dilation and erosion is shown. In Figure 4.8, a cross sectional view of gray level opening and closing is shown.

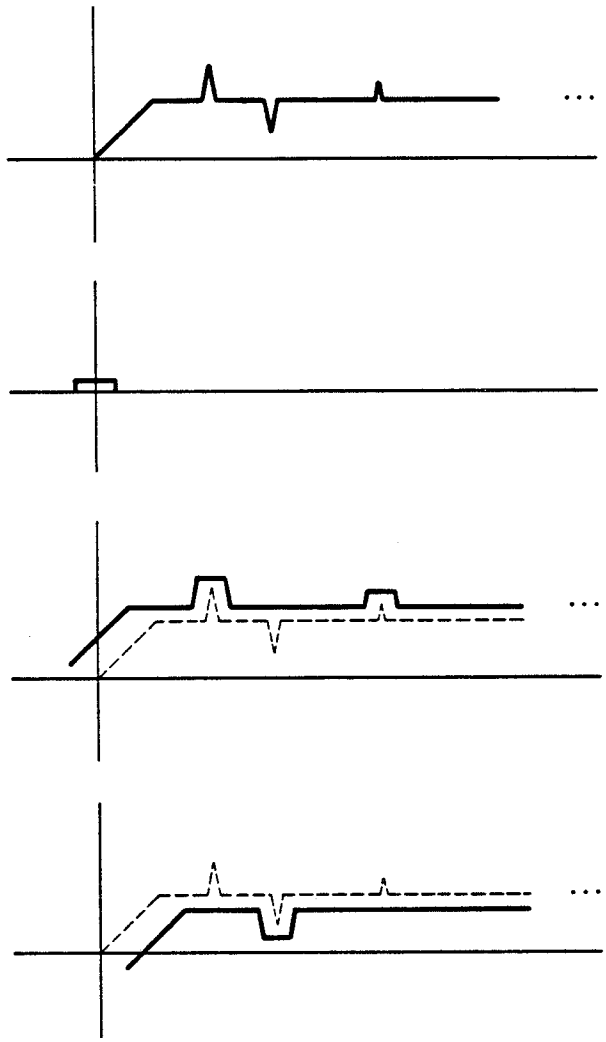

Figure 4.7 Gray level dilation and erosion. Downward, beginning at the top: image f, structuring element g, dilation of f by g, erosion of f by g. (adapted from [22])

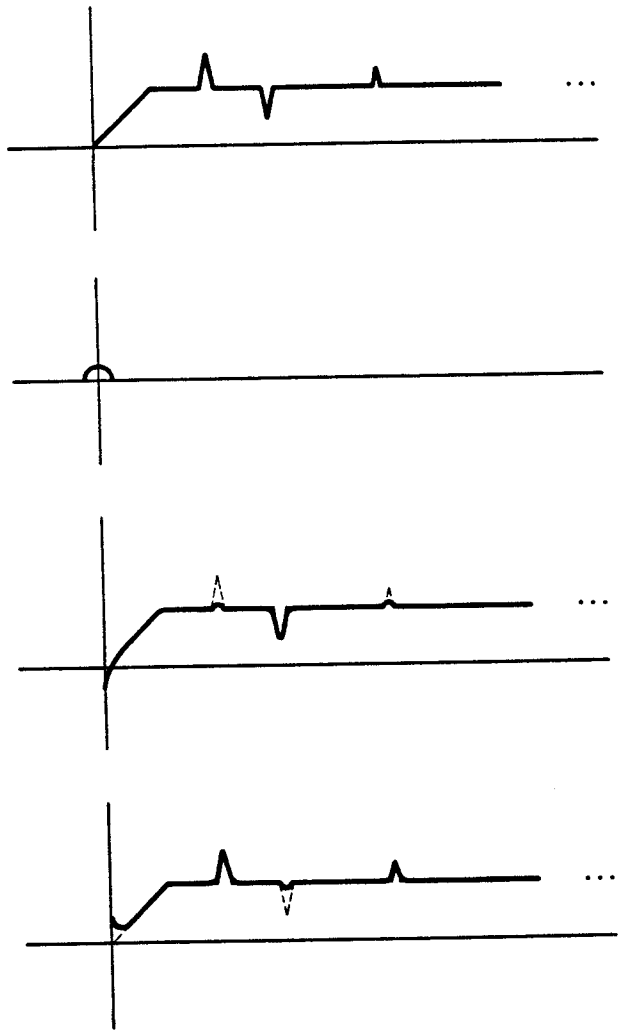

Figure 4.8 Gray level opening and closing. Downward, beginning at top: image f, structuring element g, opening of f by g, closing of f by g. (adapted from [22])

Note how the opening tends to remove positive spikes into which the structuring element cannot fit, whereas the closing tends to remove negative spikes into which the structuring element cannot fit. In Figure 4.9, a cross sectional view shows the different result obtained between opening then closing, $(f_g)^g$, versus closing then opening, $(f^g)_g$, using f and g from Figure 4.8.

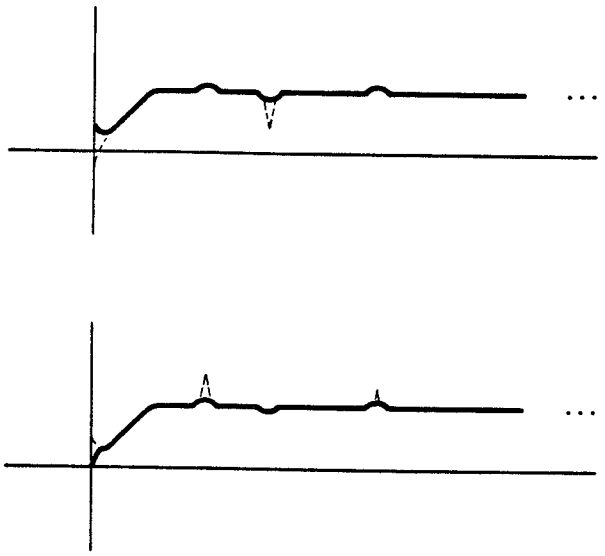

Figure 4.9 Different result between opening then closing (*top*) versus closing then opening (*bottom*). (adapted from [22])

We presented the previous discussion to familiarize the reader with the properties of mophological operators used in image processing. We now proceed to describe the morphological filter algorithm which is designed specifically to mitigate the image degradation due to the hostile nuclear environment.

4.3.2.3 The Filter Algorithm

Recall that we desire a filter algorithm which can remove γ noise, Gaussian white noise, and a structured background from a corrupted image. Several nonlinear filters, such as the median filter, seem well suited to noise removal, yet do not provide an acceptable method for background removal. It has been shown that morphological filters, due to their discrimination based on

shape, are capable of removing both noise and a structured background from signals and images [12],[15],[58].

Noise removal using morphological operators was shown in Figure 4.8, where positive spikes smaller than the structuring element were removed by opening, and negative spikes smaller than the structuring element were removed by closing. Thus for removal of bipolar noise, both an opening and a closing are required. From Figure 4.9 we can see that the result is dependent upon the order of the operations. The best filtered estimate of the original image is produced when the image is processed by both open-close and close-open, then averaging the two results [12]. However, this amount of processing can be prohibitive; using either open-close or close-open alone provides satisfactory perfromance for most types of images [12]. Since the target images consist of high valued target pulses on a low valued background, the open-close method should provide slightly better results [54]. If the structuring element is designed with a shape and size such that it "fits" inside the smallest target pulses but not within the largest noise spikes, then the open-close will eliminate the noise spikes while preserving the target pulses. Since the target pulses are modeled as positive Gaussian pulses, effective structuring elements should be small positive dome shaped objects.

As previously discussed, an effective technique of background normalization is to remove the target pulses while preserving the structured background, then subtracting this background estimate from the original target image. The result is an image containing target pulses but no structured background [58]. Since morphological operators can discriminate between various shapes in an image compared to the structuring element, we can use morphology to achieve background normalization [12],[15],[58]. We design a structuring element with a size and shape such that it cannot "fit" within the largest target pulse, yet closely follow the contours of the background. Because we know a priori that the targets consist only of positive going pulses, this background estimate can be performed with a single opening of the image [15]. It has been shown that the best background estimate is achieved when the opening is performed on an image in which the noise has already been removed [12].

Thus an effective filter algorithm for corrupted target images would include and opening and closing to remove the noise, an opening to estimate the background, and a subtraction to perform the background nomalization. This algorithm is shown in Figure 4.10. With properly designed structuring elements for each stage, this filter should provide effective negation of the image corruption due to the hostile nuclear environment. Further, like the other nonlinear filters discussed, this morphological filter should produce little adverse

effect on the CSORR of the processed image.

In this chapter we have identified and examined candidate image enhancement algorithms which may enable us to overcome the image degradation expected from nuclear detonations. The morphological filter algorithm presented seems to hold the greatest promise, since it can not only remove noise, but it also can normalize a structured background. In the next chapter we present the results of testing the various image enhancement algorithms using the previously defined models.

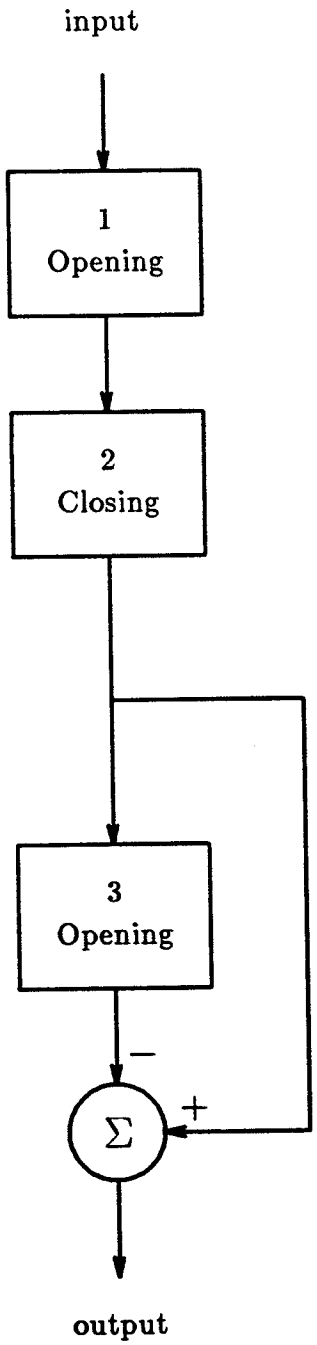

Figure 4.10 Morphological filter algorithm for corrupted target images.

CHAPTER 5
TARGET IMAGE ENHANCEMENT RESULTS

5.1 INTRODUCTION

In previous chapters, we developed models that simulate both the targets and the image corruption expected in the hostile nuclear environment. We also identified representative image enhancement algorithms that may reduce this corruption to an acceptable level. In this chapter, we present the results of testing these algorithms on various target images.†

5.2 CORRUPTED TARGET IMAGES

We created a set of twelve test images which each include three target pulses (two of which are CSOs) and various degrees of corruption. The characteristics of each image were chosen to test the algorithms for some specific result. In the nuclear environment, we cannot predict if, how, when, where, or how many warheads may penetrate the defensive screen and detonate; thus we cannot predict the exact makeup of the actual image degradation. Therefore, we seek algorithms which provide acceptable image enhancement for any combination of image corruption. Recall that this corruption may be in the form of impulsive noise, Gaussian white noise, structured backgrounds, or various combinations of these. While it is likely to have impulsive noise present without a structured background if few detonations take place, the existence of a structured background means the effects of several detonations are probably interacting, and thus the presence of impulsive noise is guaranteed. As discussed in Section 3.5, Gaussian white noise is always present in realizable systems.

The twelve test images are all 256×256 pixels and are quantized to 256 levels, as discussed in Section 2.2. The definitions of type 1 and type 2 impulsive noise, P_e for both types, Gaussian white noise and the associated σ, and

† While the tables of results are embedded in the text, the figures all are placed at the end of the chapter to make visual comparisons easier.

the characteristics of the structured background can be found in Chapter 3. Recall that the structured background was specified by three values: the linear slope (in levels/pixel), the sinusoidal peak amplitude (in levels), and the sinusoidal period (in pixels). The various parameters used to create the test images are listed in Table 5.1.

Table 5.1
Test Image Parameters

Image #	CSORR	Type 1 P_1	Type 2 P_2	Gaussian σ	Structured Background	Testing For
0	0.25	0	0	0	none	MSE comparison
1	0.48	0	0	0	none	changed CSORR
2	0.25	0	0	32	none	Gaussian noise removal
3	0.25	0.05	0.005	0	none	γ noise removal
4	0.25	0.10	0.010	0	none	γ noise removal
5	0.25	0.25	0.025	0	none	γ noise removal
6	0.25	0.50	0.050	0	none	γ noise removal
7	0.25	0	0	0	A†	background removal
8	0.25	0	0	0	B‡	background removal
9	0.25	0.05	0.005	32	A	combined scenario
10	0.25	0.10	0.010	32	A	combined scenario
11	0.25	0.25	0.025	32	A	combined scenario
12	0.25	0.50	0.050	32	A	combined scenario

† Values used for A: slope = 0.4; peak amplitude = 32; period = 128

‡ Values used for B: slope = 0.4; peak amplitude = 16; period = 32

While most test images were used to evaluate how well an algorithm removed a single form of corruption, images 9-12 combined all the forms together, with image 12 representing the worst case scenario.

Two different structured backgrounds were used for testing. In Table 5.1 they are designated A and B. Background A is identical to that of Figure 3.4 and represents a reasonable estimate of a typical structured background viewed at a medium distance from the sensors. Background B, however, represents a structured background for which the period is close to the combined width of the CSO pulses.

The numbers listed in Table 5.1 were obtained by quantitative estimates of the predicted environment and qualitative visual judgement as to the

perceived image corruption. The maximum P_e used in test images 6 and 12, for example, is the level at which the target pulses are completely obscured by the impulsive noise; this most likely represents greater corruption from γ noise than would exist in reality.

5.3 FIGURES OF MERIT

When evaluating the performance of image enhancement algorithms, each is measured relative to predefined criteria. The individual criterion may be measured qualitatively or quantitatively. Quantitative measurements, known as *figures of merit*, allow more precise comparisons between algorithms, but in dealing with images we should not ignore qualitative judgements. We shall, therefore, include qualitative remarks where appropriate when discussing the image enhancement results.

As discussed in Section 1.2, the criteria for this application include maximum reduction in the effects of the nuclear environment; minimal change in target size, shape, or position; minimal increase in the CSORR; and acceptable time and space complexity for real time image processing. Of these, we omit specific measurements for time and space complexity since there are too many variations of hardware and software to make any significant comparisons.

The most important figure of merit for comparing the various algorithms is a measure of the degree to which the image corruption is removed. Some type of comparison between the uncorrupted target image and the processed test image must be made. While several measures of this type have been developed, the most common figure of merit is the mean square error (MSE). This is the measure we chose for this study. If the original image is designated s_{xy}, and the processed test image is designated $\hat{s}_{xy}$, then the MSE is given by

$$\text{MSE} = \frac{1}{N} \sum_{x,y \in s_{xy}} (\hat{s}_{xy} - s_{xy})^2 \tag{5.1}$$

where N is the number of pixels in s_{xy} and $\hat{s}_{xy}$. Qualitative judgements concerning image quality are also included, since in some instances MSE alone can be misleading. For example, if most of the noise were removed, yet the height of the target pulses were reduced, the MSE would indicate an overly pessimistic result.

Any change in target size or shape was determined from visual inspection of displays and plots of the images. In general, this change was directly proportional to the degree of corruption in the image. Possible changes in

apparent target location were tested by determining the coordinates of the target pulse centers before and after processing; none of the algorithms tested resulted in any appreciable change, except for the median/morphological hybrid discussed later. The final figure of merit compares how much the CSORR changes due to processing. Once again, this is simply a matter of measuring the value before and after processing.

These figures of merit were determined for all the test images processed by the various image enhancement algorithms. The pertinent results are presented and analyzed in the next section.

5.4 ANALYSIS OF THE RESULTS

We wish to provide the basis for a comparative analysis of the various filter algorithms. We first present the test results concerning removal of Gaussian noise and γ noise (type 1 and type 2 impulsive noise), followed by background normalization (removal of the structured background). Then, we present the test results from applying the most promising enhancement techniques to images with all the types of corruption combined. This most closely simulates the hostile nuclear environment. We follow this with measurements of CSO blurring for all the filter types considered.

The notation used in the following sections for the morphological filters is defined as follows:

M1 Opening with a 3×3 gray level structuring element, followed by closing with a 5×5 gray level structuring element (see Figure 5.1) for noise removal. These structuring elements were empirically derived.

M33 Opening with a 33×33 gray level structuring element (see Figure 5.2) to remove targets and thus estimate the background.

M49x3 Opening with a 49×3 gray level structuring element (see Figure 5.2) to remove targets and thus estimate the background.

The design of structuring elements for morphological filters is still a somewhat *ad hoc* process. We estimated which image shape parameters we wished to preserve and which ones we wished to eliminate, and from these parameters designed a group of structuring elements. After examining the results, we modified the structuring elements to optimize the desired enhancement effects. While this may seem to be an imprecise method of designing structuring elements, it produces the best results at this point in time. As the statistical properties of morphological filters become more defined in the future, the design of

structuring elements will become more exact.

The results of this study are presented in the following four sections, making use of tabular, graphical, and pictorial representations as appropriate.

5.4.1 Noise Removal

The figure of merit relative to the noise removal performance of a filter can be separated into two parameters: removal of Gaussian noise, and removal of γ noise.

The first parameter tested was the ability of each algorithm to suppress Gaussian noise. While the level of corruption due to Gaussian noise should not be a significant problem, it still represents a form of image degradation that will be present even if no nuclear detonations occur. We are therefore interested in how each filter suppresses Gaussian noise. Test image 2 was processed by each filter type; the MSE between the processed image and the uncorrupted standard (test image 0) was then determined. This data is shown in Table 5.2. Note: the signal to noise ratio of test image 2 is $\simeq$ 12 dB.

Table 5.2
Gaussian Noise Removal Results
(using Test Image 2)

Filter Type	MSE
None	499.8
Gaussian $\sigma = 1.0$	160.9
Averaging 3×3	186.4
α-Trimmed Mean 3×3	122.4
Median 3×3	85.7
Min/Max 3×3	0.8
M1	18.3

While all the filter types significantly reduced the Gaussian noise, the min/max and morphological filters yielded the best results.

The second parameter tested was the ability of each filter to suppress γ noise. Variations of each filter type were used to process test images 3-6. See Table 5.1 for the level of γ noise corruption (due to type 1 and type 2 impulsive noise models) for these test images. The MSE between the processed image and the standard uncorrupted test image 0 was computed. This data is shown

in Table 5.3. The nonlinear filters are definitely superior at reducing the effects of γ noise. While the 3×3 min/max filter appears to be superior to the 3×3 median filter in terms of MSE, this is a case where qualitative observations are important.

Table 5.3
Gamma Noise Removal Results

Filter Type	Test Image	MSE
None	3	1707.5
None	4	3272.0
None	5	8131.9
None	6	15429.2
Gaussian $\sigma = 1.0$	3	176.5
Gaussian $\sigma = 2.0$	3	77.1
Averaging 7×7	3	84.6
Averaging 11×11	3	65.9
α-Trimmed Mean 3×3	4	152.0
α-Trimmed Mean 3×3	5	1084.7
Median 3×3	5	193.1
Median 7×7	5	0.7
Median 7×7	6	50.7
Median 11×11	6	8.4
Min/Max 3×3	5	33.1
Min/Max 3×3	6	90.1
M1	4	0.8
M1	5	6.3
M1	6	385.2

The min/max filter suppresses the impulsive spikes more effectively, at the cost of breaking the target pulses up into many smaller objects when the image corruption is high, as in test images 5 and 6. This effect would tend to confound the CSO problem. Larger window sizes cause the min/max filter to nearly eliminate the target pulses. The median filter, however, is nearly as effective at removing the gamma noise without adversely affecting the target pulses. Thus the median filter is the most desirable of the ranked order filters.

The morphological filter produces results comparable to the median filter until the degree of image corruption becomes very high, as in test image 6. At this level of γ noise, the target pulses are corrupted to such a degree that the

structuring elements cannot effectively eliminate the spikes. The net result is that the target pulses are broken up into several smaller pulses. This effect is similar to that observed for the min/max filter; however, it is not a problem until very high levels of image corruption (as in test image 6) exist.

5.4.2 Background Normalization

As indicated in Chapter 4, most filter types cannot acceptably remove a structured background from an image. Only morphological filters, which respond to the shape of the image, can selectively remove the target pulses without undue distortion of the structured background. Because of this, we test only the morphological approach to background normalization described in Section 4.3.2.3.

Two test images (7 and 8) were used to measure the effectiveness of the background normalization procedure. Test image 7 represents the most reasonable guess for a typical structured background in the nuclear environment. Test image 8 presents more of a challenge; its period was designed to approach the combined width of the CSO pulses. A structuring element large enough to remove the pulses is too large to follow the shape of this type of background. Whether this situation would actually exist in the nuclear environment is unknown; we only wish to demonstrate the limitation inherent in this approach to background normalization.

Two structuring elements were used to estimate the background. The 33×33 dome shaped structuring element, being symmetrical, is designed to yield the best estimate for any orientation of the background. The 49×3 oblong structuring element is designed to yield the optimum estimate when the orientation of the background is known. Using compass points as reference, if the structured background consists of a sinusoidal variation from east to west, then the long dimension of the structuring element is oriented north to south. It is designed such that its long dimension allows removal of the target pulses, but is short dimension is small enough to follow the shape of the background variations.

The test images were processed by performing an opening with the indicated structuring element. The MSE between the processed image and the standard uncorrupted test image 0 was computed. This data is shown in Table 5.4. See Figure 5.3 for a comparison of the background estimate of test image 7 using both structuring elements. Note that the dome shaped structuring element results in some visible error in the estimate, while the oblong structuring element yields an almost perfect estimate. However, the oblong structuring element is useful only when the background orientation is known a priori.

Table 5.4
Background Normalization Results

Filter Type	Test Image	MSE
None	7	7669.1
None	8	5358.5
M33	7	93.1
M33	8	171.7
M49x3	7	0.1
M49x3	8	0.2

Two observations are apparent from the table. First, the shorter period background is much more difficult to estimate and thus normalize. Second, while the 33×33 structuring element yields very good results, the 49×3 structuring element is nearly ideal when it is properly aligned with the background. Unfortunately, it is highly unlikely that we can expect to have much a priori knowledge about the orientation of the structured background. Thus the 33×33 structuring element would most likely be the best choice.

5.4.3 Combined Scenario

The ultimate test of the filter algorithms is how well they can negate the combined effects of the hostile nuclear environment. Test images 9-12 were used for this; they include corruption from γ noise, Gaussian white noise, and a structured background. Three stage morphological filters (opening then closing for noise removal, then opening for background estimation) were tested using both 33×33 and 49×3 structuring elements for background normalization.

Morphological filters tend to become less effective for γ noise removal at very high levels of image corruption, whereas median filters do not. Because of this, we also tested a hybrid filter consisting of a 7×7 median filter (for noise removal) followed by a morphological opening using the 33×33 structuring element (for background normalization). The 7×7 window size was chosen as a tradeoff between noise suppression and processing speed. This hybrid filter is similar to the filter of Section 4.3.2.3; we simply replaced the initial opening and closing with the median filter.

We computed the MSE between the processed images and the standard uncorrupted test image 0 for comparison. This data is shown in Table 5.5.

Table 5.5
Combined Noise Removal and
Background Normalization Results

Filter Type	Test Image	MSE
None	9	11911.9
None	10	13446.4
None	11	18265.9
None	12	25726.1
M1/M33	9	90.5
M1/M33	10	109.3
M1/M33	11	156.6
M1/M33	12	631.0
M1/M49x3	9	26.2
M1/M49x3	10	42.4
M1/M49x3	11	99.4
M1/M49x3	12	563.9
Median 7×7/M33	9	87.3
Median 7×7/M33	10	98.6
Median 7×7/M33	11	153.1
Median 7×7/M33	12	411.5

The results of processing test images 9-12 with the morphological filters M1/M33 and M1/M49x3 are shown in Figures 5.4 through 5.8.

The noise removal and background normalization algorithm using morphological filters provides very good results until the image corruption is very high, as in test image 12. This level of γ noise exceeds the ability of the morphological opening-closing to effectively discriminate between target pulses and noise spikes. However, Figure 5.8 shows that the pulses are clearly visible after processing.

The hybrid median/morphological filter did not yield much better results. While the median filter removes γ noise alone very effectively, it appears that when a structured background is present the "flat" window of the median filter causes enough distortion (sort of a "staircase" effect) to significantly reduce the ability of the morphological opening to accurately estimate the background. This greatly lessens the effectiveness of the algorithm. Further, this filter distorted the shape of the pulses in test image 12 to such a degree that a

targeting system using the pulse center of mass for localization would be rendered useless. This characteristic of the hybrid median/morphological filter would make it a poor choice for a strategic defense system.

Since the level of corruption represented by test image 12 most likely exceeds that which could be expected in the field, the morphological filter M1/M33 is the best general solution to the problem of noise removal and background normalization.

5.4.4 CSO Blurring

As stated previously, filter algorithms that tend to blur CSOs together, and thus increase the CSORR, will make it more difficult for the system to discriminate between the CSOs. We tested each algorithm by processing test image 1 (having a CSORR of 0.48) with each filter type, then recorded the average value of the two CSO peaks and the valley between them. The CSORR was then computed using Equation (2.5). This data is shown in Table 5.6.

Table 5.6
CSO Blurring Results
(using Test Image 1)

Filter Type	peak	valley	CSORR
None	125.3	60.5	0.48
Gaussian $\sigma = 1.0$	122.0	60.0	0.49
Gaussian $\sigma = 2.0$	117.3	61.0	0.52
Averaging 3×3	123.3	60.0	0.49
Averaging 11×11	107.3	63.0	0.59
α-Trimmed Mean 3×3	123.3	60.0	0.49
Median 3×3	123.7	60.5	0.49
Median 11×11	110.0	62.0	0.56
Min/Max 3×3	125.0	60.5	0.48
M1	124.0	62.5	0.50
M1/M33	98.0	40.5	0.41
Median 7×7/M33	93.0	40.0	0.43

As indicated, the linear filters tend to increase the CSORR more for a given window size. Recall that the Gaussian filter has a window size of approximately 7σ. The change in CSORR due to the background normalization stage

(M33) is dependent upon the fidelity of the background estimation. Note that this can lead to the unexpected result of the processed CSORR being better than the input CSORR. From Table 5.6 we see that the M1/M33 morphological filter, recommended for noise removal and background normalization, is also acceptable with regard to its effect on the CSORR.

In this chapter we have presented the results of testing the various image enhancement algorithms. Using the models that simulate image corruption due to nuclear detonations, we found that the best solution to the problem of reducing this corruption appeared to be the three stage morphological filter described in Section 4.3.2.3. The next chapter provides a brief summary of this study and presents our conclusions.

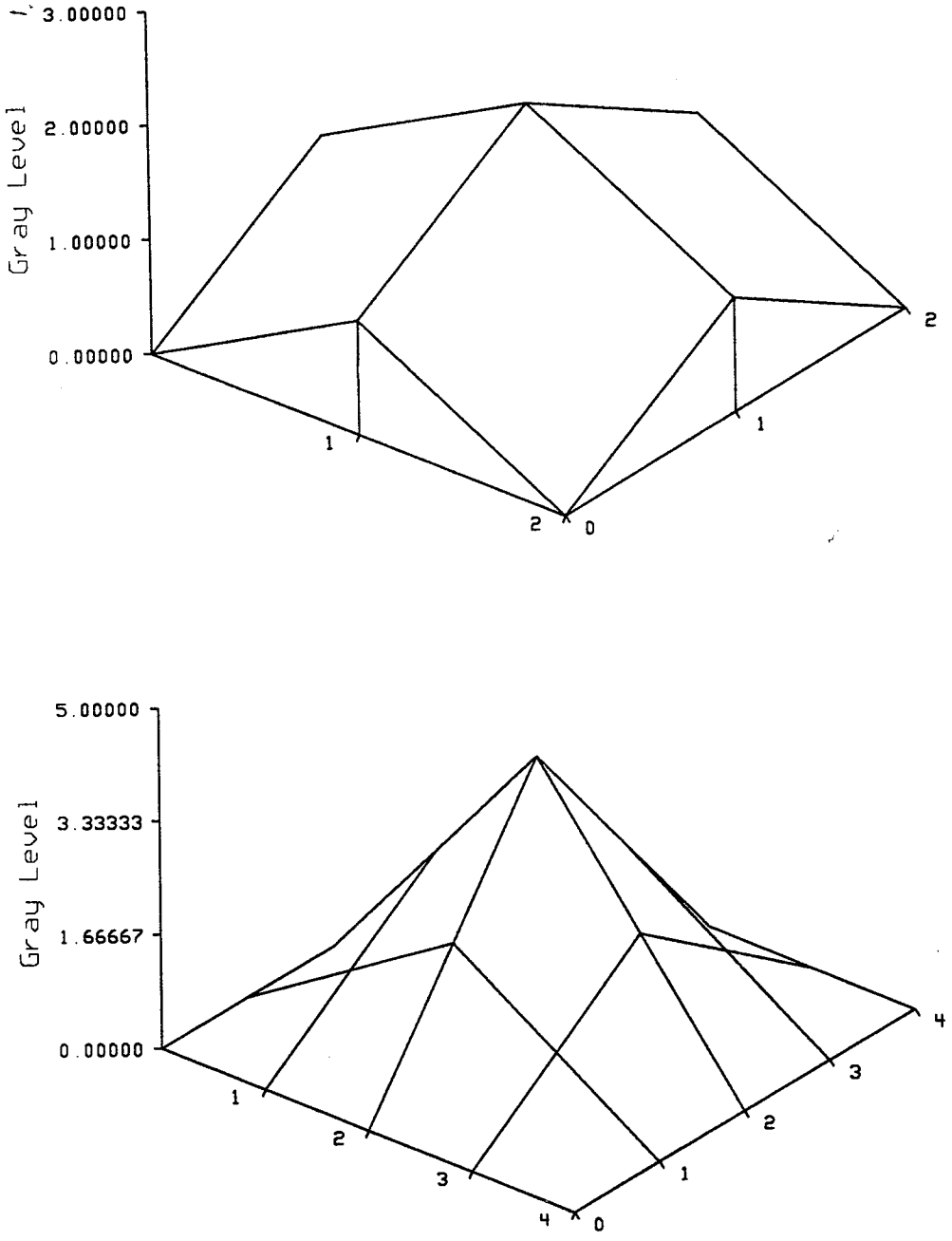

Figure 5.1 Structuring elements for noise removal. *Top*: 3×3. *Bottom*: 5×5. Despite the appearance of the graphs, these structuring elements are centered about the origin.

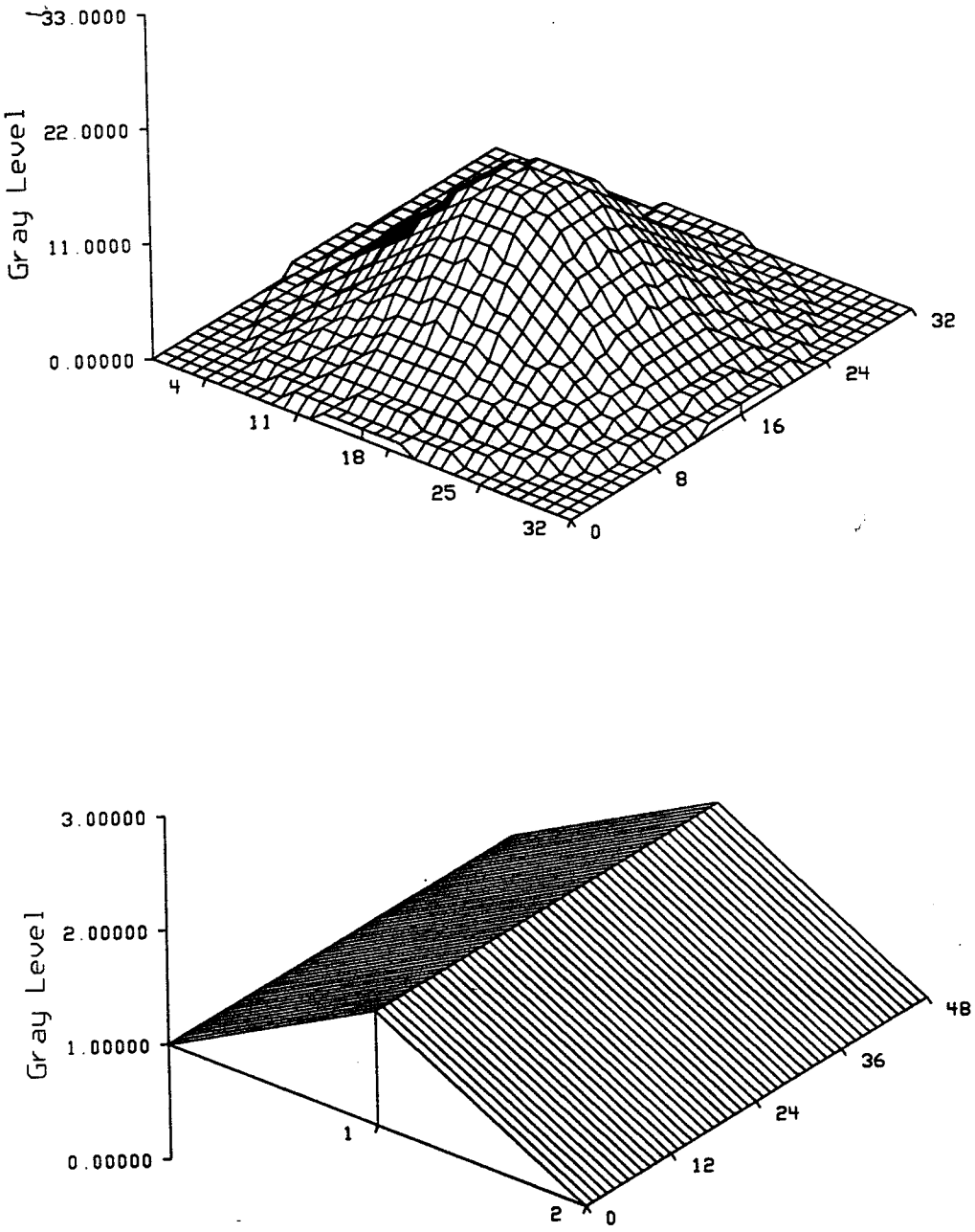

Figure 5.2 Structuring elements for background estimation. *Top*: 33×33. *Bottom*: 49×3. Despite the appearance of the graphs, these structuring elements are centered about the origin.

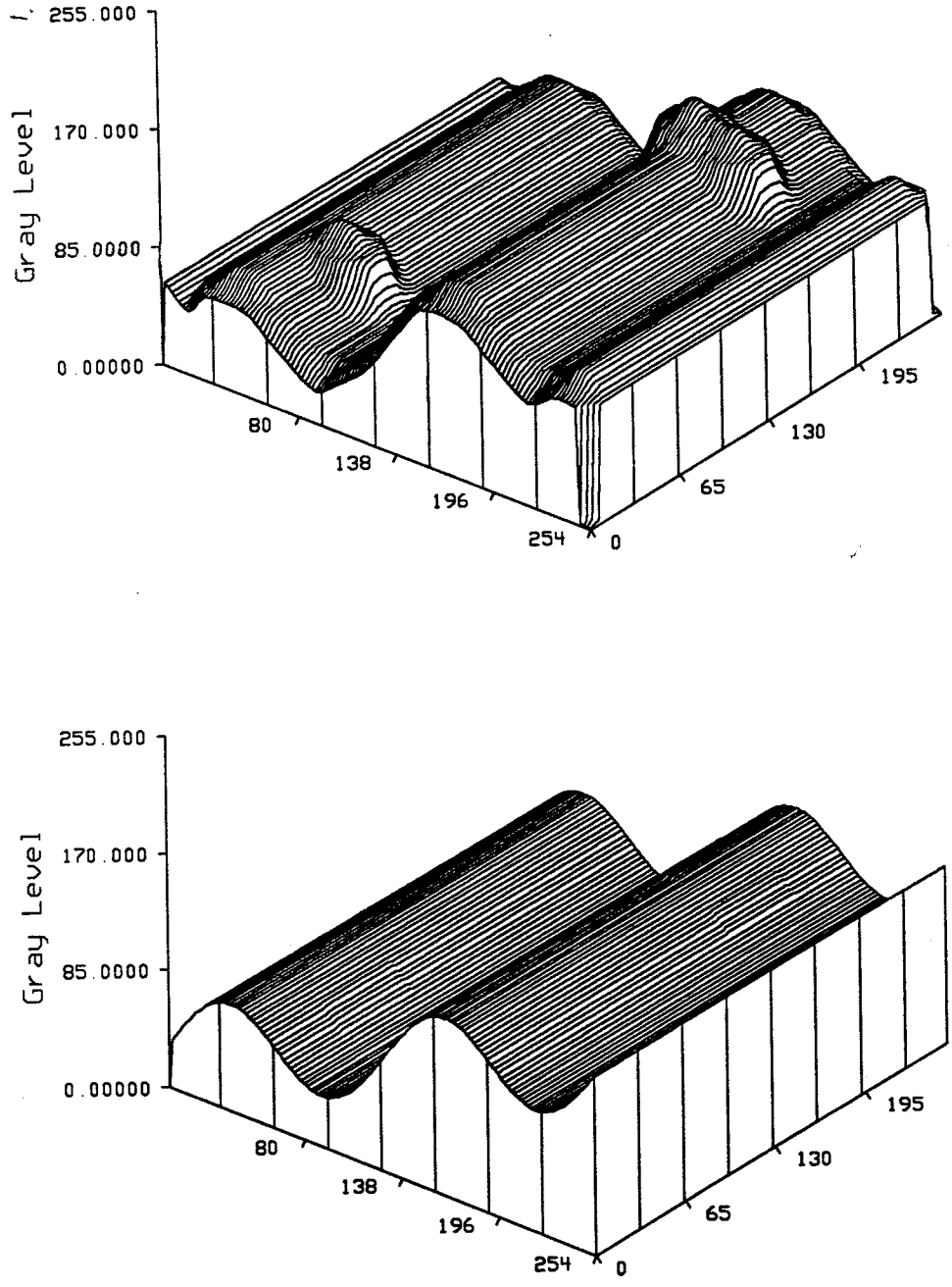

Figure 5.3 Two background estimates. *Top*: Opening using 33×33 dome shaped structuring element. *Bottom*: Opening using 49×3 oblong shaped structuring element.

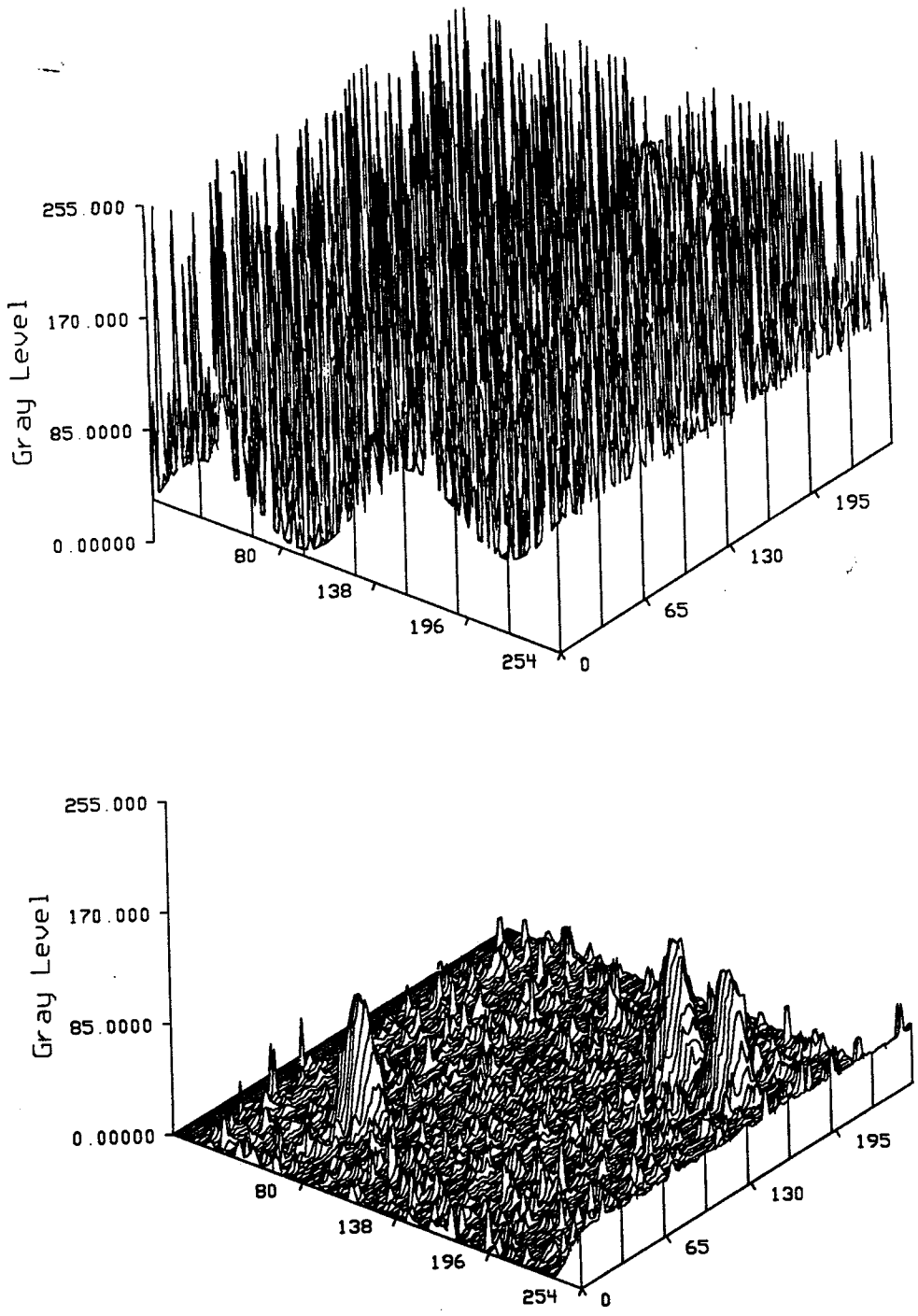

Figure 5.4 Test image 9 before and after processing. *Top*: Original image. *Bottom*: Image after processing by M1/M33.

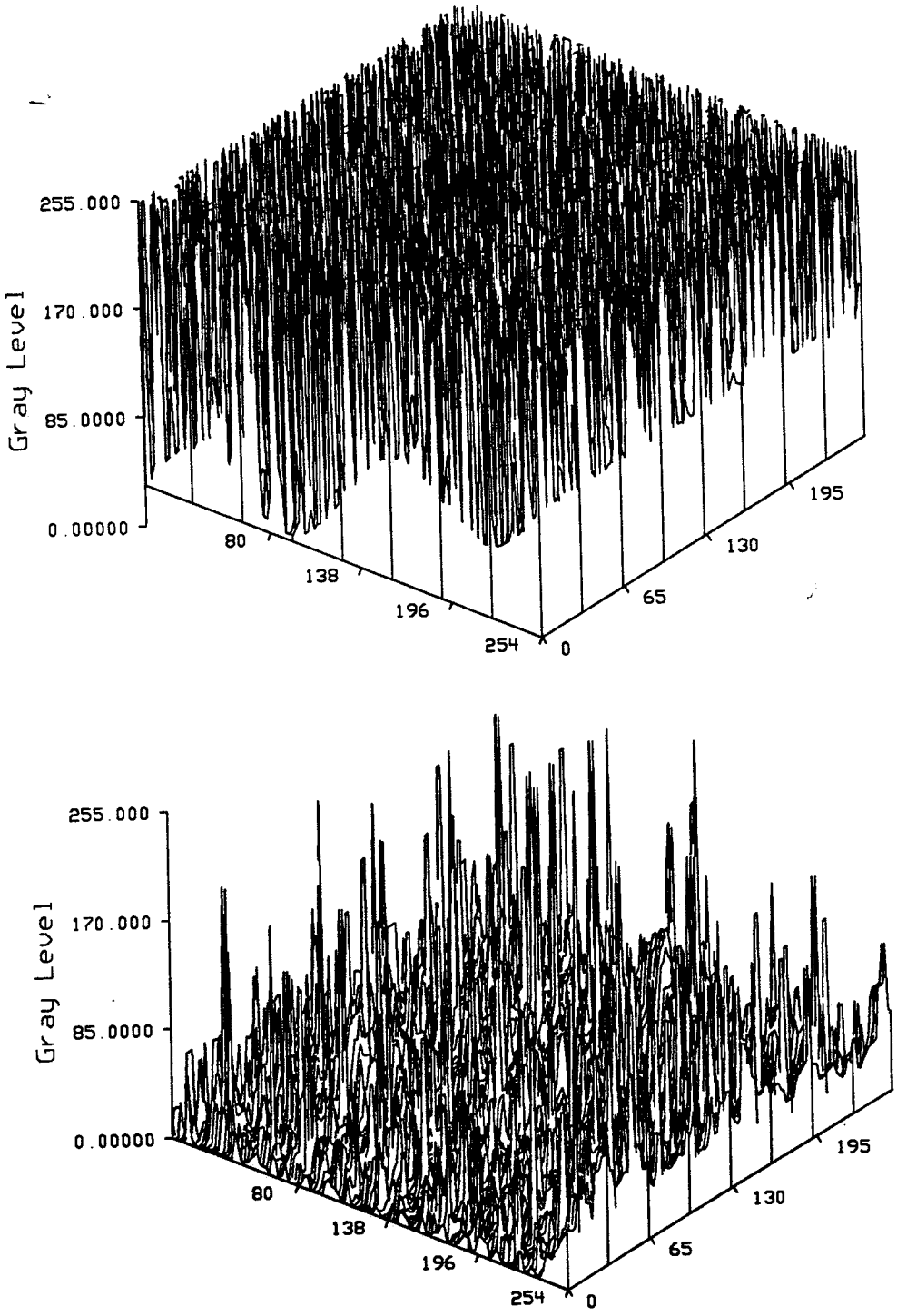

Figure 5.5 Test image 12 before and after processing. *Top*: Original image. *Bottom*: Image after processing by M1/M33.

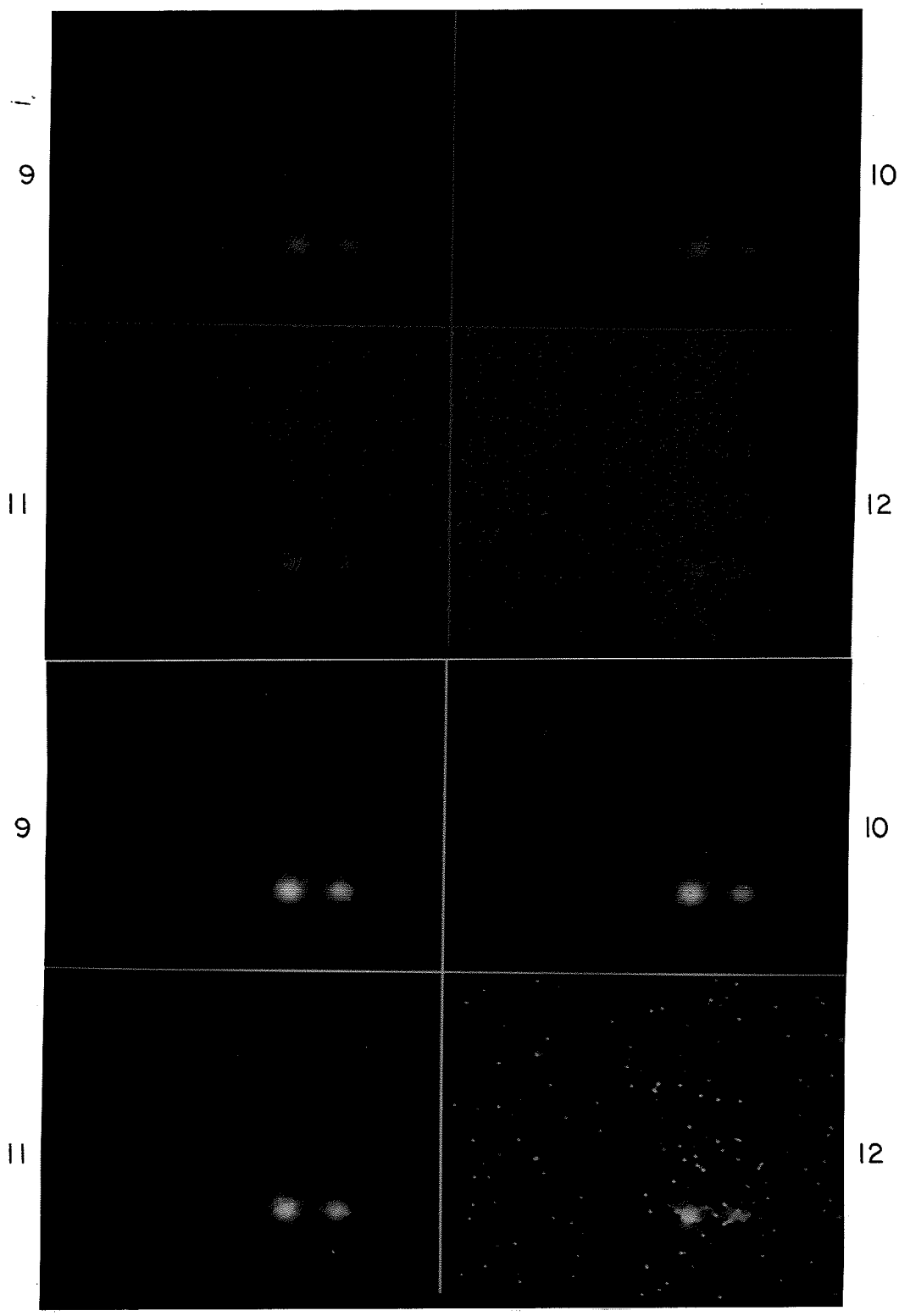

Figure 5.6 Photos of initial processing of test images 9-12. *Top*: Original images. *Bottom*: Images after opening and closing by M1.

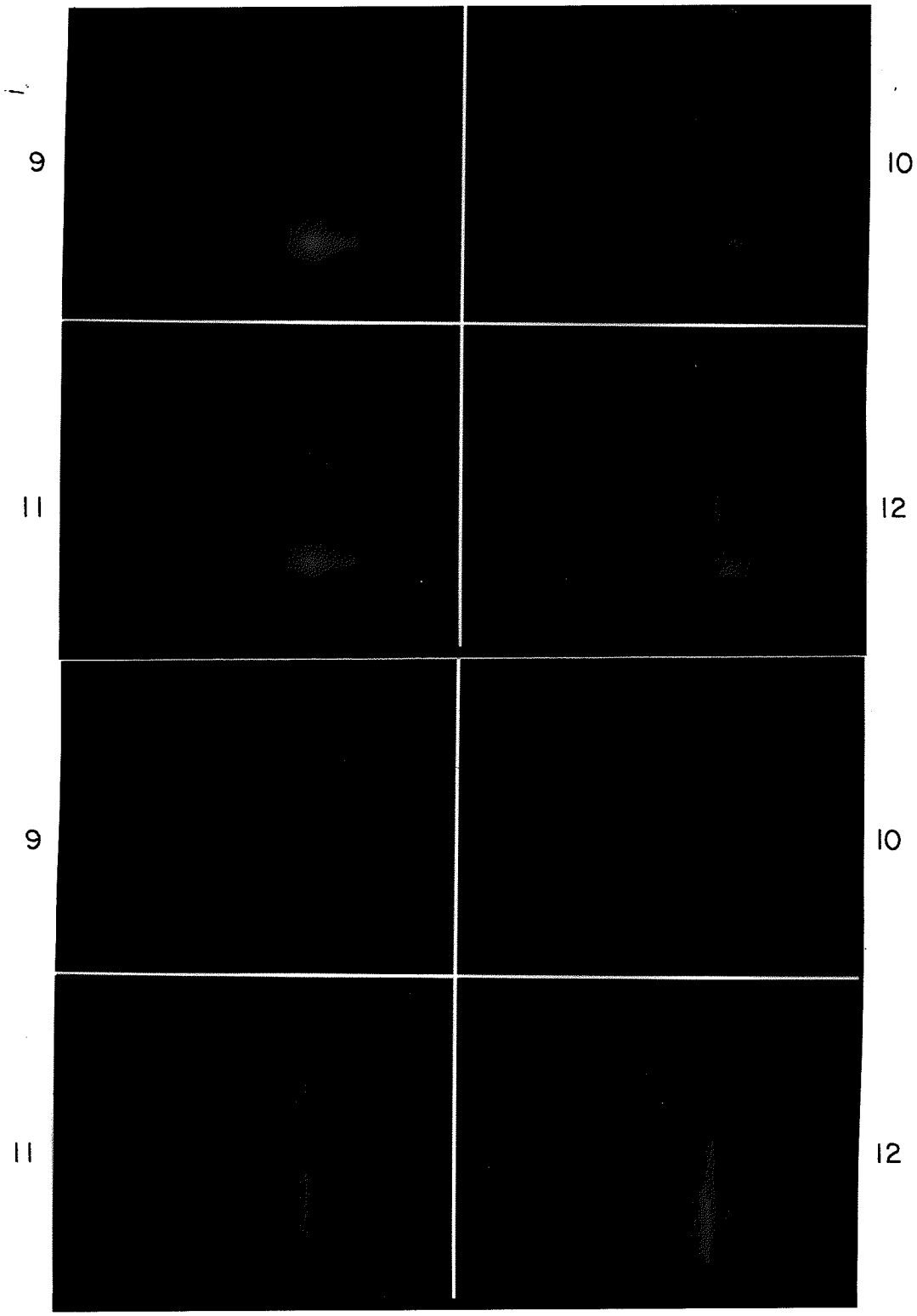

Figure 5.7 Photos of background estimates for test images 9-12. *Top*: Background estimate using M33. *Bottom*: Background estimate using M49x3.

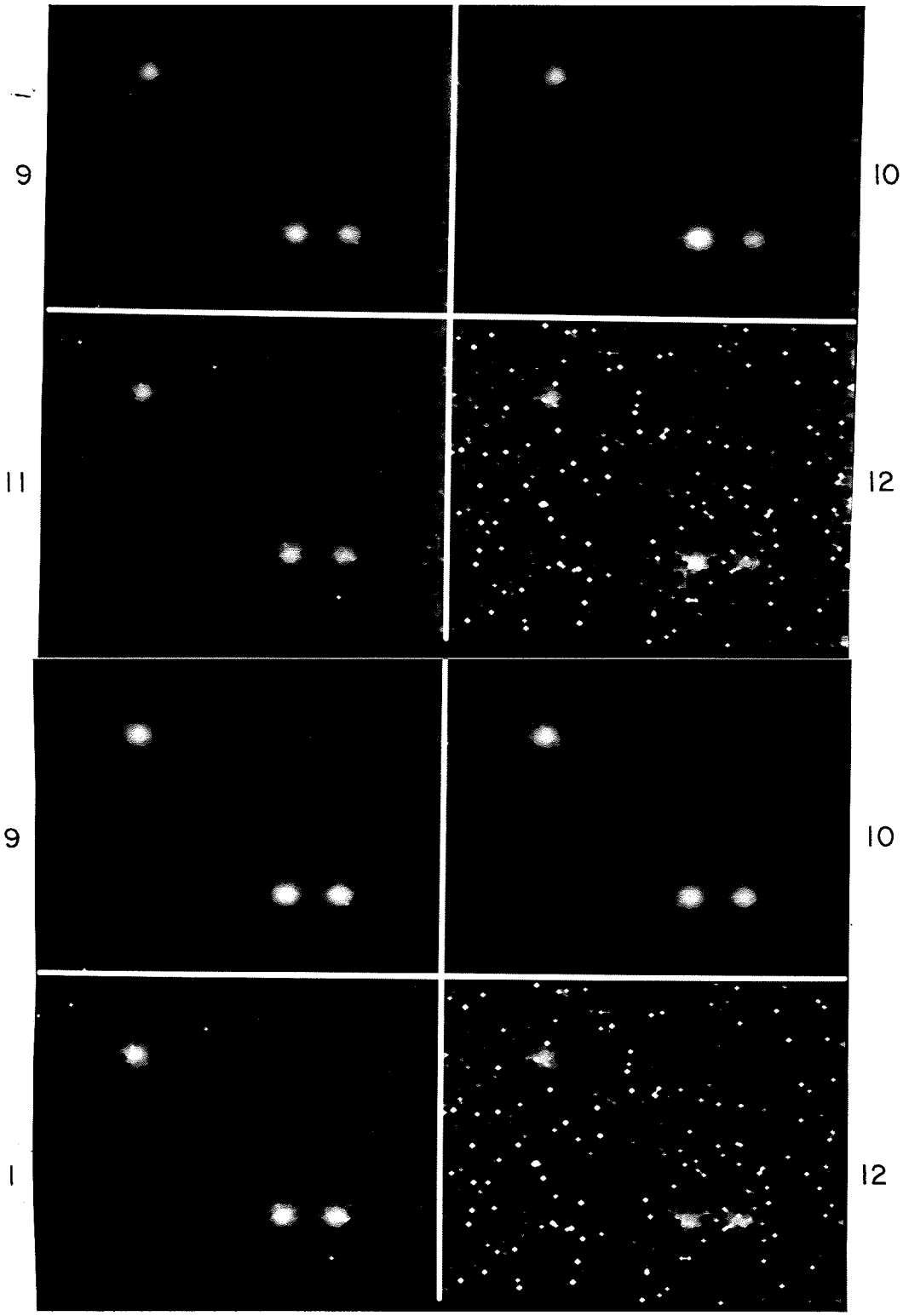

Figure 5.8 Photos of final processing of test images 9-12. *Top*: Processed by M1/M33. *Bottom*: Processed by M1/M49x3.

CHAPTER 6
SUMMARY AND CONCLUSIONS

6.1 REVIEW OF THIS STUDY

In this study, we developed a realistic model for incoming nuclear warheads as they would appear to LWIR sensors. We showed that these warheads, being distant endoatmospheric objects radiating infrared radiation, could be modeled as two dimensional Gaussian pulses. Further, we described how closely spaced objects (CSOs) require special consideration.

Next, we developed four models representing the image corruption that would exist in the hostile nuclear environment. In order of presentation, these models are described below.

Type 1 impulsive noise:

Bipolar impulsive noise due to γ radiation and limited hardware malfunctions, with spike intensity limited by the dynamic range of the system. Modeled using Bernoulli trials on each pixel of the image.

Type 2 impulsive noise:

Bipolar impulsive noise due to γ radiation and limited hardware malfunctions, with random spike amplitude and polarity. Modeled using Bernoulli trials on each bit of every pixel in the image.

Structured background:

Spatial structuring of the atmospheric transmittance due to interactions between multiple nuclear detonations. Modeled using a linear ramped sinusoidal function.

Gaussian white noise:

Noise due to natural and man-made phenomena unrelated to the nuclear environment, and therefore present even in the absence of nuclear detonations. Modeled using a zero mean Gaussian distribution.

These models were combined into an aggregate noise model which was used to

corrupt the simulated target images.

Various image enhancement algorithms were then introduced and discussed as to their anticipated ability to reduce or negate the effects of the nuclear environment. In order of presentation, these algorithms are listed below.

Linear Methods

- Gaussian Filter
- Averaging Filter

Nonlinear Methods

- Alpha-Trimmed Mean Filter
- Median Filter
- Min/Max Filter
- Morphological Filters

It was predicted that the linear filters would perform poorly in the presence of impulsive noise, while the nonlinear filters would be effective at suppressing both impulsive and Gaussian noise. The morphological filter, by incorporating an additional stage for background normalization, would possibly be able to remove a structured background from the image.

We then tested each algorithm using the corrupted target images, and presented the results. As predicted, the linear filters failed to remove impulsive noise effectively. They also introduced significant image blurring which had detrimental effects on the CSORR. The nonlinear filters significantly reduced the image corruption due to both impulsive noise and Gaussian white noise with much less effect on the CSORR. And most importantly, the morphological filter was able to remove the structured background from the image as well. A hybrid median/morphological filter was tested as an alternative to the morphological filter, but tended to distort the shape of the target pulses. Thus the morphological filter, using the implementation described in Section 4.3.2.3, is the best overall choice for enhancing target images corrupted by the hostile nuclear environment.

6.2 CONCLUDING REMARKS

As stated above, morphological filters provide an effective solution to the combined problem of noise removal and background normalization. However, one of the ramifications of applying any filtering operation is the danger that

important elements of the image may be inadvertently removed. Given this caveat, the key to successful implementation of the morphological filters used in this study is careful choice of the structuring elements. For the noise removal stage, the structuring element is designed to be small enough that the smallest anticipated target will be preserved, yet large enough that the variations and impulses due to noise are removed. This may involve tradeoffs between early warhead detection and maximum acceptable noise in the image. For the background normalization stage, the structuring element is designed to be large enough that the largest anticipated target (including targets combined as CSOs) will be removed, yet small enough to follow the contours of any structured background that may occur in the image. If the periodicity of the background approaches the size of the largest target pulse, background normalization begins to fail. Here, the tradeoff is more critical: a poorly designed structuring element for this stage would not only fail to normalize the structured background, but could also prevent the system from ever detecting a legitimate target. This would occur if the background estimate included a legitimate target pulse, which would consequently be subtracted out of the image.

While it may seem obvious, we point out that even with the best image enhancement algorithms, the target image must contain target pulses. Some effects from nuclear detonations, such as large clouds of dust and other particulate matter, may reduce the atmospheric transmittance to such a degree that the targets will not show up at all. Multiple sensor locations and multiple sensor platforms (ground, aircraft, and space) would be one approach to circumvent this problem.

Further research is recommended for refining the models developed in this study, using empirical test data where possible. In particular, the incorporation of actual sensor parameters, plus experimentally derived γ noise probabilities and structured backgrounds would be beneficial. Further refinement of optimum structuring element design for the background normalization stage is recommended; nonsymmetrical shapes can provide more robust performance for structured backgrounds, even with low periodicity, but presently require an unrealistic amount of a priori knowledge. A valuable continuation of this study would be an extension to four dimensions by including temporal information; multi-frame sequences include much more data about the targets. Exploration of using image phase information instead of or in addition to amplitude information is also recommended; this might yield even better results than we have demonstrated here. Further research is also recommended to explore the potential of combining several signal processing stages (such as noise and background removal, target detection, classification, and tracking)

into fewer stages using the geometric discrimination of morphological operators.

In conclusion, it appears that properly designed morphological filters can provide us with the ability to effectively negate the image corruption due to the hostile nuclear environment. However, further research is required before we can fully realize this potential and apply it to a reliable strategic defense system.

LIST OF REFERENCES

LIST OF REFERENCES

[1] Arce, G. R., "Median filters: theory and applications," Ph.D. Dissertation, Purdue University, West Lafayette, IN, Aug. 1982.

[2] Arce, G. R., N. C. Gallagher, and T. A. Nodes, "Median filters: theory for one- and two- dimensional filters," in *Advances in Computer Vision and Image Processing*, ed. T. S. Huang, vol. 2, pp. 89-166, JAI Press, Greenwich, CT, 1986.

[3] Arce, G. R. and R. L. Stevenson, "On the synthesis of median filter systems," *IEEE Trans. Circuits Syst.*, vol. CAS-34, no. 4, pp. 420-429, Apr. 1987.

[4] Arce, G. R. and M. P. Mcloughlin, "Theoretical analysis of the max/median filter," *IEEE Trans. Acoust., Speech, Signal Processing*, vol. ASSP-35, no. 1, pp. 60-69, Jan. 1987.

[5] Bednar, J. B. and T. L. Watt, "Alpha-trimmed means and their relationship to median filters," *IEEE Trans. Acoust., Speech, Signal Processing*, vol. ASSP-32, no. 1, pp. 145-153 , Feb. 1984.

[6] Bendat, J. S. and A. G. Piersol, *Random Data,* 2nd ed., John Wiley & Sons, New York, 1986.

[7] Bernstein, R., "Adaptive nonlinear filters for simultaneous removal of different kinds of noise in images," *IEEE Trans. Circuits Syst.*, vol. CAS-34, no. 11, pp. 1275-1291, Nov. 1987.

[8] Billingsley, P., *Probability and Measure,* John Wiley & Sons, New York, 1979.

[9] Bovik, A. C., T. S. Huang, and D. C. Munson, Jr., "A generalization of median filtering using linear combinations of order statistics," *IEEE Trans. Acoust., Speech, Signal Processing*, vol. ASSP-31, no. 6, pp. 1342-1349, Dec. 1983.

[10] Canny, J., "A computational approach to edge detection," *IEEE Trans. Pattern Anal. Machine Intell.*, vol. PAMI-8, no. 6, pp. 679-698, Nov. 1986.

[11] Carlson, A. B., *Communication Systems,* 2nd ed., McGraw-Hill, New York, 1975.

[12] Chu, C. H. and E. J. Delp, "Impulsive noise suppression and background normalization of electrocardiogram (EKG) signals using morphological operators," *IEEE Trans. Biomedical Engineering* (submitted for publication), Jan. 1988.

[13] Cooper, G. R. and C. D. McGillem, *Modern Communications and Spread Spectrum,* McGraw-Hill, New York, 1986.

[14] Cooper, G. R. and C. D. McGillem, *Probabilistic Methods of Signal and System Analysis,* 2nd ed., Holt, Rinehart and Winston, New York, 1986.

[15] Delp, E. J. and N. C. Gallagher, Internal Technical Report, Gallagher Associates, Inc., West Lafayette, IN, Oct. 1987.

[16] Dudgeon, D. E. and R. M. Mersereau, *Multidimensional Digital Signal Processing,* Prentice-Hall, Englewood Cliffs, NJ, 1984.

[17] Feher, K., *Digital Communications: Satellite/Earth Station Engineering,* Prentice-Hall, Englewood Cliffs, NJ, 1983.

[18] Fitch, J. P., E. J. Coyle, and N. C. Gallagher, "Median filtering by threshold decomposition," *IEEE Trans. Acoust., Speech, Signal Processing*, vol. ASSP-32, no. 6, pp. 1183-1188, Dec. 1984.

[19] Fitch, J. P., E. J. Coyle, and N. C. Gallagher, "Threshold decomposition of multidimensional ranked order operations," *IEEE Trans. Circuits Syst.*, vol. CAS-32, no. 5, pp. 445-449, May 1985.

[20] Gallagher, N. C. and G. L. Wise, "A theoretical analysis of the properties of median filters," *IEEE Trans. Acoust., Speech, Signal Processing*, vol. ASSP-29, no. 6, pp. 1136-1141, Dec. 1981.

[21] Ghose, R. N., *EMP Environment and System Hardness Design,* Don White Consultants, Inc., Gainesville, VA, 1984.

[22] Giardina, C. R. and E. R. Dougherty, *Morphological Methods in Image and Signal Processing,* Prentice-Hall, Englewood Cliffs, NJ, 1988.

[23] Giffen, R. B., *US Space System Survivability: Strategic Alternatives for the 1990s,* National Security Affairs Monograph Series, National Defense University Press, Washington, DC, 1982.

[24] Glasstone, S. and P. J. Dolan (eds.), *The Effects of Nuclear Weapons,* 3rd ed., prepared by US Department of Defense, available from Superintendent of Documents, US Government Printing Office, Washington, DC, 1977.

[25] Gonzalez, R. C. and P. Wintz, *Digital Image Processing,* Addison-Wesley, Reading, MA, 1977.

[26] Goodman, J. W., *Introduction to Fourier Optics,* McGraw-Hill, New York, 1968.

[27] Grimson, W. E. L., *From Images to Surfaces,* MIT Press, Cambridge, MA, 1981.

[28] Hamming, R. W., *Digital Filters,* 2nd ed., Prentice-Hall, Englewood Cliffs, NJ, 1983.

[29] Haralick, R. M., S. R. Sternberg, and X. Zhuang, "Image analysis using mathematical morphology," *IEEE Trans. Pattern Anal. Machine Intell.*, vol. PAMI-9, no. 4, pp. 532-550, July 1987.

[30] Hunt, B. R., "Digital image processing," in *Applications of Digital Signal Processing*, ed. A. V. Oppenheim, pp. 169-237, Prentice-Hall, Englewood Cliffs, NJ, 1978.

[31] Justusson, B. I., "Noise reduction by median filtering," in *Proc. 4th Int. Joint Conf. on Pattern Recognition*, 1978.

[32] Kim, V. and L. Yaroslavskii, "Rank algorithms for picture processing," *Computer Vision, Graphics, and Image Processing*, vol. 35, pp. 234-258, 1986.

[33] Lantuejoul, C. and J. Serra, "M-filters," in *Proc. ICASSP-82* (Paris), pp. 2063-2066, May 1982.

[34] Lee, K. S. H. (ed.), *EMP Interaction: Principles, Techniques, and Reference Data,* Hemisphere Publishing, Washington, DC, 1986.

[35] Maragos, P. A., "A unified theory of translation-invariant systems with applications to morphological analysis and coding of images," Ph.D. Dissertation (Tech. Rep. DSPL-85-1), Georgia Institute of Technology, Atlanta, GA, July 1985.

[36] Maragos, P. A. and R. W. Schafer, "A unification of linear, median, order-statistics, and morphological filters under mathematical morphology," in *Proc. ICASSP-85* (Tampa, FL), pp. 34.8.1-34.8.4, Mar. 1985.

[37] Maragos, P. A. and R. W. Schafer, "Applications of morphological filtering to image analysis and processing," in *Proc. ICASSP-86* (Tokyo), pp. 2067-2070, Apr. 1986.

[38] Marr, D., *Vision,* W. H. Freeman and Company, San Francisco, 1982.

[39] Messenger, G. C. and M. S. Ash, *The Effects of Radiation on Electronic Systems,* Van Nostrand Reinhold, New York, 1986.

[40] Miller, J. H. and J. B. Thomas, "Detectors for discrete-time signals in non-gaussian noise," *IEEE Trans. Inform. Theory*, vol. IT-18, no. 2, pp. 241-250, Mar. 1972.

[41] Nakagawa, Y. and A. Rosenfeld, "A note on the use of local min and max operations in digital picture processing," *IEEE Trans. Syst., Man, Cybern.*, vol. SMC-8, no. 8, pp. 632-635, Aug. 1978.

[42] National Research Council, *The Effects on the Atmosphere of a Major Nuclear Exchange,* National Academy Press, Washington, DC, 1985.

[43] Nodes, T. A. and N. C. Gallagher, "The output distribution of median type filters," *IEEE Trans. Commun.*, vol. COM-32, no. 5, pp. 532-541, May 1984.

[44] Oppenheim, A. V. and R. W. Schafer, *Digital Signal Processing,* Prentice-Hall, Englewood Cliffs, NJ, 1975.

[45] Ott, H. W., *Noise Reduction Techniques in Electronic Systems,* John Wiley & Sons, New York, 1976.

[46] Papoulis, A., *Systems and Transforms with Applications in Optics,* McGraw-Hill, New York, 1968.

[47] Papoulis, A., *Probability, Random Variables, and Stochastic Processes,* 2nd ed., McGraw-Hill, New York, 1984.

[48] Pau, L. F. and M. Y. El Nahas, *An Introduction to Infrared Image Acquisition and Classification Systems,* Research Studies Press Ltd., Letchworth, Hertfordshire, England, 1983.

[49] Pipes, L. A. and L. R. Harvill, *Applied Mathematics for Engineers and Physicists,* 3rd ed., McGraw-Hill, New York, 1970.

[50] Rabiner, L. R. and B. Gold, *Theory and Application of Digital Signal Processing,* Prentice-Hall, Englewood Cliffs, NJ, 1975.

[51] Rosenfeld, A. and A. C. Kak, *Digital Picture Processing, vol. 1,* 2nd ed., Academic Press, Orlando, FL, 1982.

[52] Seiler, G. S., *Strategic Nuclear Force Requirements and Issues,* Rev. ed., (Research Rep. AU-ARI-82-1), Air University Press, Maxwell AFB, AL, 1983.

[53] Serfling, R. J., *Approximation Theorems of Mathematical Statistics,* John Wiley & Sons, New York, 1980.

[54] Serra, J., *Image Analysis and Mathematical Morphology,* Academic Press, London, 1982.

[55] Shapiro, S. S. and A. J. Gross, *Statistical Modeling Techniques,* Marcel Dekker, Inc., New York , 1981.

[56] Silva, L. F., "Radiation and instrumentation in remote sensing," in *Remote Sensing: The Quantitative Approach,* ed. P. H. Swain and S. M. Davis, pp. 21-135, McGraw-Hill, New York, 1978.

[57] Snyder, D. L., *Random Point Processes,* John Wiley & Sons, New York, 1975.

[58] Sternberg, S. R., "Biomedical image processing," *Computer*, vol. 16, no. 1, pp. 22-34, Jan. 1983.

[59] Stevenson, R. L. and G. R. Arce, "Morphological filters: statistics and further syntactic properties," *IEEE Trans. Circuits Syst.*, vol. CAS-34, no. 11, pp. 1292-1305, Nov. 1987.

[60] Werman, M. and S. Peleg, "Min-max operators in texture analysis," *IEEE Trans. Pattern Anal. Machine Intell.*, vol. PAMI-7, no. 6, pp. 730-733, Nov. 1985.